nanomaterials

MDPI

Review

N-Heterocyclic Carbene-Functionalized COFs for Heterogeneous Catalysis: From Metal-Free Organocatalysis to Metal-NHC and Nanostructured Systems

Hamid Azizollahi [1], Amir Khojastehnezhad [2,*], Faezeh Bazrafshan [1] and Mohamed Siaj [2,*]

[1] Department of Chemistry, University of Utah, Salt Lake City, UT 84112, USA
[2] Department of Chemical Engineering and Biotechnological Engineering, Faculty of Engineering, Université De Sherbrooke, Sherbrooke, QC J1K 2R1, Canada
* Correspondence: khoa7829@usherbrooke.ca (A.K.); mohamed.siaj@usherbrooke.ca (M.S.)

Abstract

Covalent organic frameworks (COFs) combine permanent porosity, modular composition, and spatially organized functional groups, providing a versatile platform for translating N-heterocyclic carbene (NHC) chemistry into recoverable solid catalysts. Within these materials, NHC-related functionality can operate through distinct catalytic modes: metal-free carbene or azolium sites for organocatalysis, molecular metal-NHC (M-NHC) sites within the framework, and NHC-directed metal nanoparticles or nanoclusters. This review critically examines these systems while distinguishing among free NHCs, ionic NHC precursors, molecular M-NHC complexes, and NHC-directed metal nanostructures. Construction strategies include direct polymerization of NHC- or M-NHC-containing monomers, post-synthetic installation and quaternization of azoles, base-induced carbene generation, and mild metalation of imidazolium carboxylate precursors. Metal-free systems have been applied for organic transformations and metal-containing Au-, Cu-, Ir-, Pd-, Rh-, and Ru-NHC-COFs enable thermal and photocatalytic CO_2 conversion, C–C cross-coupling, C–H amidation, N–H insertion cascade cyclization, asymmetric oxidation-aldol relay catalysis, and H_2O_2 production. Particular emphasis is placed on crystallinity and porosity changes after modification, active-site identification, cooperative catalysis, charge-transfer behavior, catalytic efficiency, recyclability, and metal leaching. Across these catalyst classes, performance depends on carbene-generation chemistry, metal speciation, pore accessibility, framework stability, and the spatial arrangement of active sites. Future progress requires scalable synthesis, durable linkages, standardized catalytic reporting, rigorous identification of active species, greater use of earth-abundant metals, and expansion toward asymmetric and industrially relevant transformations.

Keywords: covalent organic frameworks; N-heterocyclic carbenes; porous materials; metal-NHC complexes; heterogeneous catalysis; photocatalysis

Check for updates

Academic Editor: Hui Huang

Received: 3 November 2026
Revised: 23 November 2026
Accepted: 24 November 2026
Published: 28 November 2026

Copyright: © 2026 by the authors. Licensee MDPI, Basel, Switzerland. This article is an open access article distributed under the terms and conditions of the Creative Commons Attribution (CC BY) license.

1. Introduction

Covalent organic frameworks (COFs) are crystalline porous materials with tunable structures and functionalities, offering high surface areas, well-defined porosity, and diverse applications [1–6]. Framework performance is also influenced by the conditions under which the network is formed, and catalyst-assisted protocols have enabled the more rapid preparation of crystalline two- and three-dimensional imine- and azine-linked COFs under

comparatively mild conditions, while broader comparisons demonstrate that catalyst identity, reaction time, and temperature can strongly affect defect correction, crystallinity, and accessible porosity [7–9]. Their building blocks can be selected to control topology, pore dimensions, polarity, optical response, and the spatial distribution of functional groups [2,10]. These features are particularly valuable in heterogeneous catalysis, where the catalytic environment must retain active species while allowing reactants and products to move efficiently through the solid [11,12]. Unlike conventional supports, which often present chemically heterogeneous surfaces, COFs permit catalytic functions and secondary-sphere interactions to be encoded into the framework with a comparatively high degree of structural definition [2,13].

N-Heterocyclic carbene chemistry offers several complementary ways to exploit this design freedom [14–16]. Free NHCs are strongly nucleophilic organocatalysts, whereas their azolium precursors can provide ionic microenvironments, bind or activate small molecules, and serve as masked carbenes [14,17,18]. Coordination to a metal creates an additional level of reactivity because the strongly sigma-donating carbene ligand modifies metal electron density, stabilizes selected oxidation states, and can suppress migration or aggregation [19–21]. An imidazolium- or benzimidazolium-containing COF, however, should not automatically be described as an NHC catalyst, and the presence of both a metal and an azolium unit does not by itself establish an M-NHC bond [18]. Distinguishing precursor, free-carbene, ionic, molecular metal-carbene, and metallic-particle states is therefore essential for relating catalyst structure to function [22,23].

Metal-free NHC-related COFs demonstrate that catalysis can arise directly from the framework-bound organic functionality [11,24]. Thermal decarboxylation of a CO_2-protected carbene precursor produces free NHC sites for CO_2 hydrosilylation and N-formylation [18]. Base-generated NHCs in mixed-linker benzimidazole frameworks catalyze glycerol transesterification [24], whereas immobilized benzimidazolium bromide sites promote the cycloaddition of CO_2 to epoxides through an ionic rather than metal-mediated pathway [17,25,26]. Directly polymerized imidazolium-containing frameworks have also been used for Knoevenagel condensation and base-induced γ-butyrolactone synthesis [2,27,28]. Related ionic COFs with high CO_2 uptake and anion-exchange capacity further illustrate how pore-wall charge and counterion identity can regulate adsorption and local reactivity even when no metal is present [17,26,29]. Together, these studies establish metal-free organocatalysis and ionic-site catalysis as a mechanistically distinct branch of NHC-functionalized COF chemistry [11,17].

Metal incorporation substantially broadens the accessible reaction landscape [23,30]. Molecularly defined Au-, Cu-, Ir-, Pd-, Rh-, and Ru-NHC sites have been introduced either by polymerizing preformed metal-NHC monomers or by metalating COFs that contain imidazolium, benzimidazolium, or imidazolium-carboxylate precursors [20,31–39]. These materials have been investigated in CO_2 carboxylation and hydrogenation, Suzuki–Miyaura and Mizoroki–Heck coupling, C-H amidation, N-H insertion and cascade cyclization, asymmetric oxidation-aldol relay catalysis, photocatalytic CO_2 reduction, and photocatalytic H_2O_2 production [20,32,33,38]. A related construction mode uses framework-bound NHC ligands to capture metal precursors before reduction, producing confined nanoparticles or nanoclusters rather than discrete molecular M-NHC sites [22,40]. The distinction matters mechanistically: isolated coordination sites, single atoms, and metallic ensembles may all be immobilized within a COF, but they activate substrates and traverse catalytic cycles differently [23,41].

The central analytical challenge is therefore to determine which chemical species and structural features are responsible for the observed activity [2,23]. Evidence for M-NHC bond formation must be considered together with metal oxidation state, loading,

spatial distribution, and the possible formation of nanoparticles or leached homogeneous species [22]. Framework retention also requires more than the persistence of a low-angle diffraction peak [42]. This consideration is particularly important in postsynthetically modified COFs, because incorporation of new functionality may preserve the principal diffraction features while substantially changing accessible surface area, pore volume, and mass-transport characteristics [43,44]. Comparative powder X-ray diffraction and gas-sorption measurements reveal whether long-range order and nitrogen-accessible porosity survive postsynthetic modification, while microscopy, spectroscopy, hot-filtration tests, poisoning experiments, and leaching analysis help evaluate active-site integrity and catalytic heterogeneity [22,23,45]. The functional relevance of these measurements is underscored by comparisons among structurally related imine-linked COFs, for which variations in crystallinity and accessible porosity translate directly into differences in adsorption and molecular-transport performance [46]. For both metal-free and metal-containing systems, these measurements are necessary to separate genuine confinement or cooperative effects from simple immobilization and loss of accessible pore volume [30,36].

Several reviews have addressed NHC chemistry in porous materials or the broader postsynthetic modification and catalytic applications of COFs. Wang et al. surveyed NHCs and their precursors across multiple classes of porous materials, including metal–organic frameworks, porous coordination polymers, covalent organic frameworks, porous organic polymers, and porous organometallic cages [47]. Other reviews have focused more generally on COF postsynthetic modification, heterogeneous catalysis, CO_2 utilization, or photocatalysis [4,44,48–53]. However, these publications do not provide a COF-centered and active-site-resolved comparison encompassing metal-free NHC and azolium catalysts, molecular M–NHC sites, and NHC-directed nanoparticles and nanoclusters. The present review addresses this gap by critically comparing their construction strategies, changes in crystallinity and pore accessibility, active-site identification, catalytic mechanisms, metal leaching, and recyclability. Particular emphasis is placed on distinguishing experimentally established active sites from proposed or dynamically evolving catalytic species.

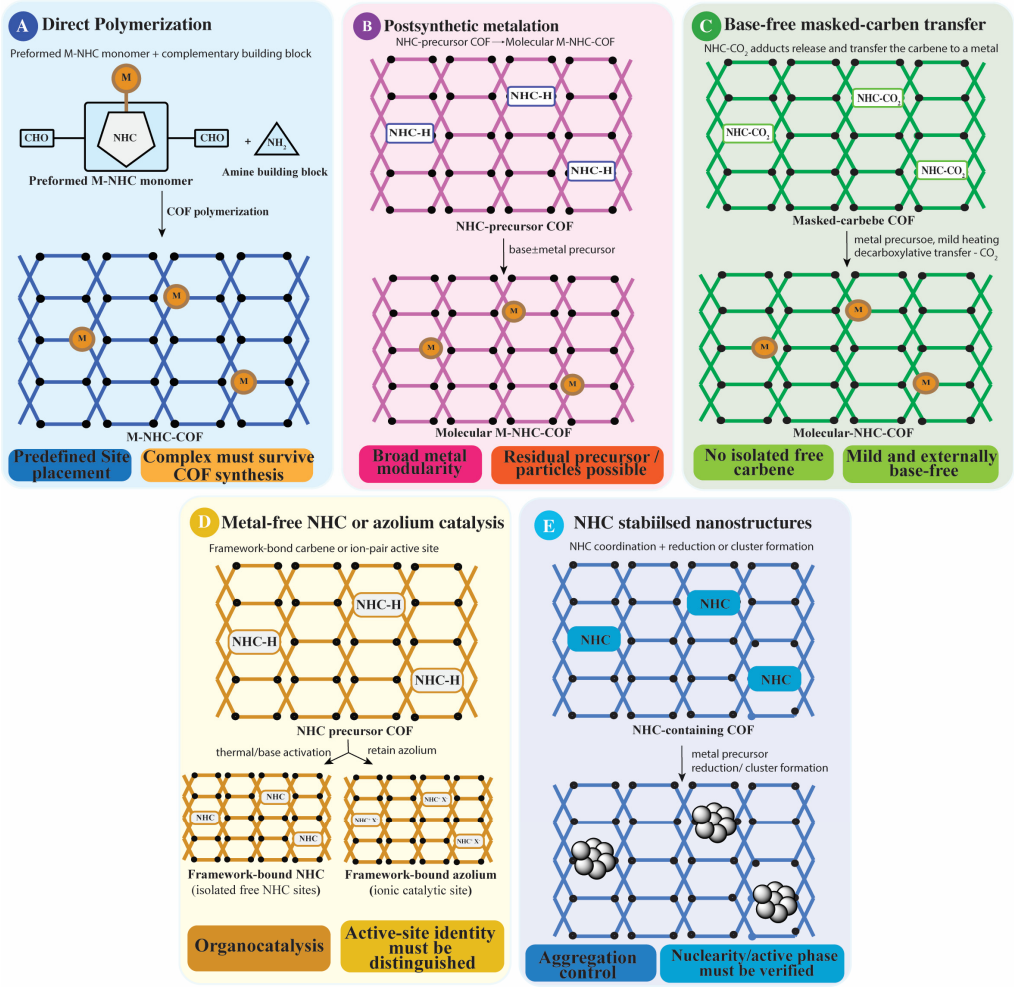
This review first compares the construction of metal-free NHC or azolium COFs, molecular M-NHC-COFs, and NHC-directed metal nanostructures. The catalytic discussion is then organized by function, covering CO_2 utilization, carbon–carbon cross-coupling, C-H and N-H functionalization, asymmetric and relay catalysis, and photocatalysis, with metal-free transformations treated alongside the corresponding construction chemistry. Cross-cutting analysis links NHC state, metal identity, topology, linkage chemistry, surface area, pore size, active-site distribution, and framework microenvironment to activity and selectivity. Particular attention is given to mechanistic evidence from spectroscopy and computation, the comparability of turnover and productivity metrics, structural retention during reuse, and resistance to metal leaching. The final sections identify the limitations that currently impede translation, including synthetic complexity, incomplete active-site assignment, demanding reaction conditions, reliance on precious metals, and limited demonstrations under continuous or preparative-scale operation.

The scope is restricted to COFs in which a framework-bound NHC, azolium precursor, or NHC-metal interaction contributes directly to catalysis, metal immobilization, or controlled formation of a catalytic metal nanostructure. Materials in which a soluble NHC is used only as a reagent during COF synthesis are treated as boundary cases rather than as NHC-functionalized catalysts.

2. Design and Construction of NHC-Functionalized COF Catalysts

NHC-functionalized COFs encompass several related but chemically distinct architectures [3,10,54–57]. In metal-free systems, an azolium group may remain as an ionic

catalytic site [25], serve as a masked carbene, or be deprotonated in situ to generate a free NHC [24,27]. In metal-containing systems, the carbene can coordinate molecular or atomically dispersed metal centers [20,31–39] or control the stabilization and spatial distribution of nanoparticles or nanoclusters [22,40]. Construction must therefore preserve framework order and pore accessibility while controlling the chemical state and spatial distribution of the NHC-derived sites [18,20,24,25,27,31,32,34,35,40]. Direct polymerization [27,29,32,33], postsynthetic installation or activation of azolium groups [18,24,25,27,34], postsynthetic metalation [20,31,35–39], and NHC-directed formation of metal nanoparticles or nanoclusters [22,40] constitute the principal construction routes [44,48,49]. Scheme 1 summarizes the metal-containing branch, whereas Figure 1 identifies the convergent evidence required to assign a credible molecular M-NHC site. For all classes, diffraction and gas-sorption measurements should be combined with chemical-state analysis, catalytic controls, filtration or leaching tests, and post-reaction characterization; no single measurement establishes framework integrity and active-site identity simultaneously [42,45,58–60].



Scheme 1. Principal construction strategies and active-site classes of NHC-functionalized COFs: (**A**) direct polymerization of premetalated M-NHC monomers; (**B**) postsynthetic metalation of NHC-precursor COFs; (**C**) base-free carbene transfer from masked NHC-CO_2 adducts; (**D**) generation of metal-free NHC or azolium catalytic sites; and (**E**) NHC-directed formation of metal nanoparticles or nanoclusters.

As summarized in Scheme 1, NHC-derived catalytic sites can be introduced into COFs through several chemically distinct routes. Direct polymerization enables predetermined placement of a preformed M–NHC complex but requires the complex to withstand the condi-

tions of framework formation. Postsynthetic metalation provides greater flexibility in metal selection, although incomplete metalation and formation of non-NHC-bound metal species must be considered. Masked NHC-CO_2 adducts offer a mild, externally base-free route to molecular M-NHC sites without isolation of a free carbene. Alternatively, framework-bound azolium groups may operate as ionic sites or generate metal-free NHC organocatalysts, whereas reduction in immobilized metal precursors can produce NHC-stabilized nanoparticles or nanoclusters. These catalyst classes must be distinguished because their active-site structures, catalytic mechanisms, and stability criteria differ substantially.

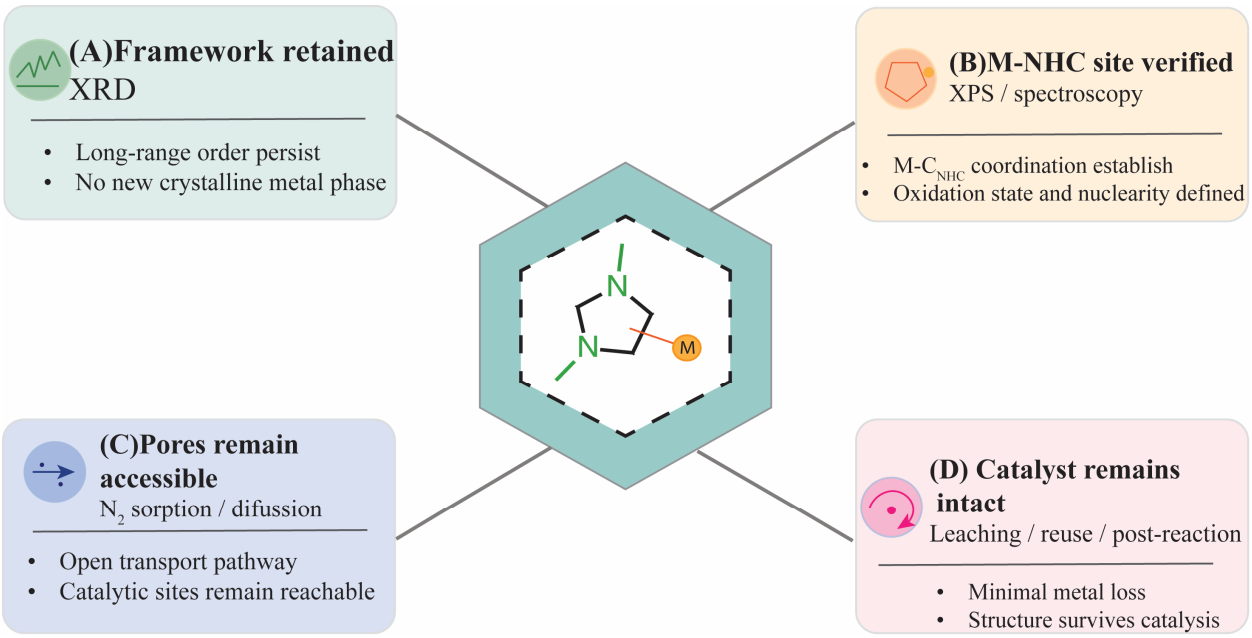


Figure 1. Complementary evidence required for structural assignment of an M-NHC-COF catalyst: (**A**) retention of framework order; (**B**) verification of M-C_NHC coordination, oxidation state, and metal nuclearity; (**C**) preservation of accessible pores and transport pathways; and (**D**) confirmation of catalyst integrity under turnover conditions.

Reliable identification of an M-NHC-COF catalyst requires convergent evidence from multiple characterization methods. PXRD can establish whether long-range framework order is retained and whether new crystalline metal-containing phases appear, whereas gas-sorption measurements reveal changes in accessible surface area and pore structure. Spectroscopic methods, particularly XPS and X-ray absorption spectroscopy, are needed to evaluate metal oxidation state, coordination environment, and nuclearity. Finally, hot-filtration experiments, quantitative metal-leaching measurements, recycling tests, and post-reaction characterization are required to assess whether the assigned active site and framework remain intact during catalysis. No single technique is sufficient to establish the complete catalyst structure.

2.1. Direct Polymerization

2.1.1. Direct Polymerization of Premetalated M-NHC Monomers

Direct polymerization enables a preformed metal-NHC complex to be incorporated during construction of the extended framework [16,21,61]. Li et al. condensed the premetalated dialdehyde TPDCA-NHC-AuCl with the triaminotriazine building block TAPT under solvothermal conditions to afford the imine-linked NHC-AuCl-COF [32]. The Au content was found to be 23.40 wt% by ICP analysis which is close to the calculated value of 24.13 wt%, and elemental mapping showed uniform distribution of Au throughout the material. The

Au $4f_{7/2}$ and Au $4f_{5/2}$ XPS signals at 85.38 and 88.92 eV, respectively, were assigned to Au(I), supporting preservation of the Au-NHC complex during framework formation. Moreover, TEM did not reveal detectable Au nanoparticles, although the absence of particles alone does not establish the coordination environment of every Au site. The resulting framework exhibited PXRD reflections at 2θ = 2.0°, 3.4°, 4.0°, 6.9°, and 8.9°, assigned to the (100), (110), (200), (220), and (140) planes, respectively. The agreement between the experimental and Pawley-refined profiles supported a two-dimensional staggered AB-stacking model [42,62,63] in the P3 space group, with unit-cell parameters of a = b = 52.0050 Å and c = 8.0140 Å (Rwp = 5.88% and Rp = 4.11%). Nitrogen sorption measurements gave a BET surface area of 139 m^2 g^{-1} and a narrow pore-size distribution centered at approximately 2.7 nm. Because no corresponding metal-free framework was reported, these measurements confirm that the directly polymerized product was crystalline and porous but do not quantify changes in crystallinity or porosity caused specifically by incorporation of the bulky Au-NHC monomer. The comparatively modest surface area may reflect steric occupation of the pores, although this interpretation cannot be verified without a matched metal-free control. The framework also permitted solid-state exchange of chloride for hexafluoroantimonate. The PXRD pattern and framework morphology remained essentially unchanged after anion exchange, whereas the BET surface area decreased moderately from 139 to 112.7 m^2 g^{-1}. Simultaneously, the water-contact angle decreased from 123 ± 2° to approximately 0°, demonstrating that counterion exchange can substantially modify the pore wettability without an evident loss of long-range framework order. This result illustrates an important advantage of direct polymerization: the metal–ligand stoichiometry is defined at the monomer stage, while the resulting framework remains amenable to secondary coordination-sphere modification. However, the method requires the preformed metal complex to withstand the acidic media, temperature, solvents, and prolonged reaction time required for COF formation (Figure 2A). The corresponding PXRD patterns and structural refinements are reported in Ref. [32].

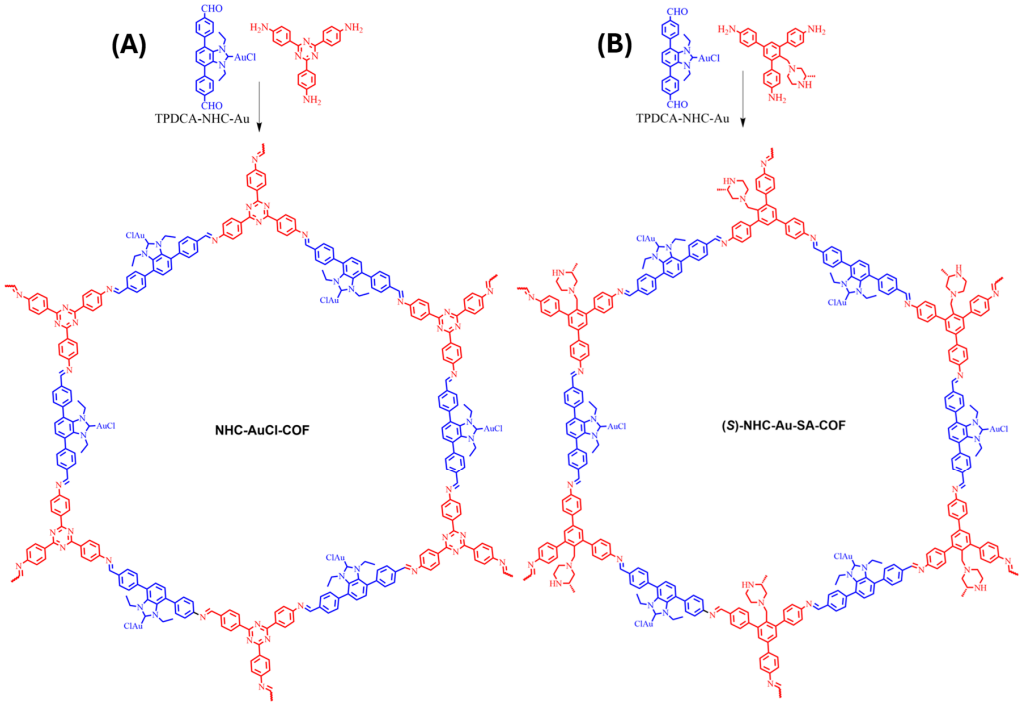


Figure 2. Synthesis of NHC-AuCl-COF (**A**). Synthesis of (*S*)-NHC-Au-SA-COF (**B**).

The direct-polymerization strategy was subsequently extended to a multifunctional chiral framework. Condensation of the premetalated TPDCA-NHC-AuCl dialdehyde with the chiral secondary-amine-containing monomer (*S*)-TAPB-MP in 1-butanol at 120 °C for three days afforded the imine-linked (*S*)-NHC-Au-SA-COF. FT-IR and solid-state ^{13}C NMR spectroscopy supported incorporation of both monomers into the framework. ICP analysis gave a Au loading of 21.94 wt%, close to the calculated value of 22.18 wt%, while the Au $4f_{7/2}$ and Au $4f_{5/2}$ XPS signals at 85.1 and 88.7 eV, respectively, were assigned to Au(I). Elemental mapping indicated that Au was distributed throughout the COF particles. Together, these results support survival and incorporation of the preformed Au(I)-NHC complex during solvothermal framework formation, although they do not independently establish identical coordination environments for every Au site. The experimental PXRD pattern showed an intense reflection at $2\theta = 2.1°$, assigned to the (100) plane, together with weaker reflections at 3.4°, 4.1°, and 5.3°, attributed to the (110), (200), and (210) planes, respectively [33]. Pawley refinement supported a two-dimensional staggered AB-stacking model [42,62,63] in the chiral P1 space group, with unit-cell parameters of a = 51.37 Å, b = 51.45 Å, and c = 8.05 Å; $\alpha = 89.88°$, $\beta = 90.02°$, and $\gamma = 120.02°$ (Rwp = 4.33% and Rp = 2.98%). Structural modeling indicated hexagon-like pores and an opposite Au···Au separation of approximately 5.1 nm. TEM further showed a layered architecture with an interlayer distance of approximately 4.05 Å, consistent with the proposed structural model [33]. Nitrogen sorption measurements gave a BET surface area of 318 $m^2\ g^{-1}$ and a narrow pore-size distribution centered at approximately 2.7 nm. The material consisted predominantly of plate-like particles with a reported hydrodynamic diameter of approximately 956 nm and remained thermally stable to about 400 °C. As with NHC-AuCl-COF, no corresponding metal-free framework with the same composition and topology was reported. Consequently, the PXRD and sorption data establish that the directly polymerized bifunctional framework was crystalline and porous but do not quantify losses in crystallinity or accessible surface area caused specifically by the Au-NHC monomer [33].

Processing (*S*)-NHC-Au-SA-COF with chitosan into a cup-shaped aerogel preserved the characteristic PXRD features of the crystalline framework but decreased the BET surface area from 318 to 162 $m^2\ g^{-1}$. This reduction indicates lower nitrogen-accessible microporosity after shaping, even though the macroscopic aerogel architecture facilitated catalyst handling and enabled gram-scale relay catalysis. The result illustrates an important practical trade-off: shaping improves recoverability and reactor compatibility but may reduce access to the intrinsic COF surface (Figure 2B). The corresponding PXRD patterns and structural refinements are reported in Ref. [33].

2.1.2. Direct Polymerization of Metal-Free NHC-Precursor Monomers

Direct polymerization can also incorporate a metal-free NHC precursor into a COF. Zhang et al. condensed the imidazolium-containing diamine NAP with tetra(p-formylphenyl)porphyrin (p-Por-CHO) in DMSO/H_2O using acetic acid at 120 °C for three days, affording the imine-linked Por-NHC-COF in 60.1% yield [27]. FT-IR spectroscopy showed attenuation of the aldehyde C=O band at 1701 cm^{-1} and appearance of an imine C=N band at 1622 cm^{-1}, supporting framework formation. The material should nevertheless be described as an imidazolium-containing NHC-precursor COF rather than a free-NHC framework [16,64]. Por-NHC-COF displayed a prominent PXRD reflection at $2\theta = 2.81°$. Comparison with simulated patterns favored eclipsed AA stacking, with unit-cell parameters of a = b = 67.8 Å and c = 36.6 Å. Because no Pawley refinement was reported, this stacking arrangement should be regarded as the most consistent structural model rather than a definitive assignment [42,62,63]. The type-IV nitrogen-sorption isotherm indicated mesoporosity, although the BET surface area was only 53.0 $m^2\ g^{-1}$. Without a structurally

matched control, this low value cannot be attributed exclusively to the imidazolium functionality. The principal PXRD features were retained after exposure to water, 12 M HCl, and strongly basic media, as well as after six catalytic cycles. However, post-treatment BET measurements were not reported. During γ-butyrolactone synthesis, KOtBu was proposed to deprotonate the imidazolium sites and generate active NHCs, but free framework-bound carbenes were not directly characterized under the reaction conditions [27] (Figure 3A).

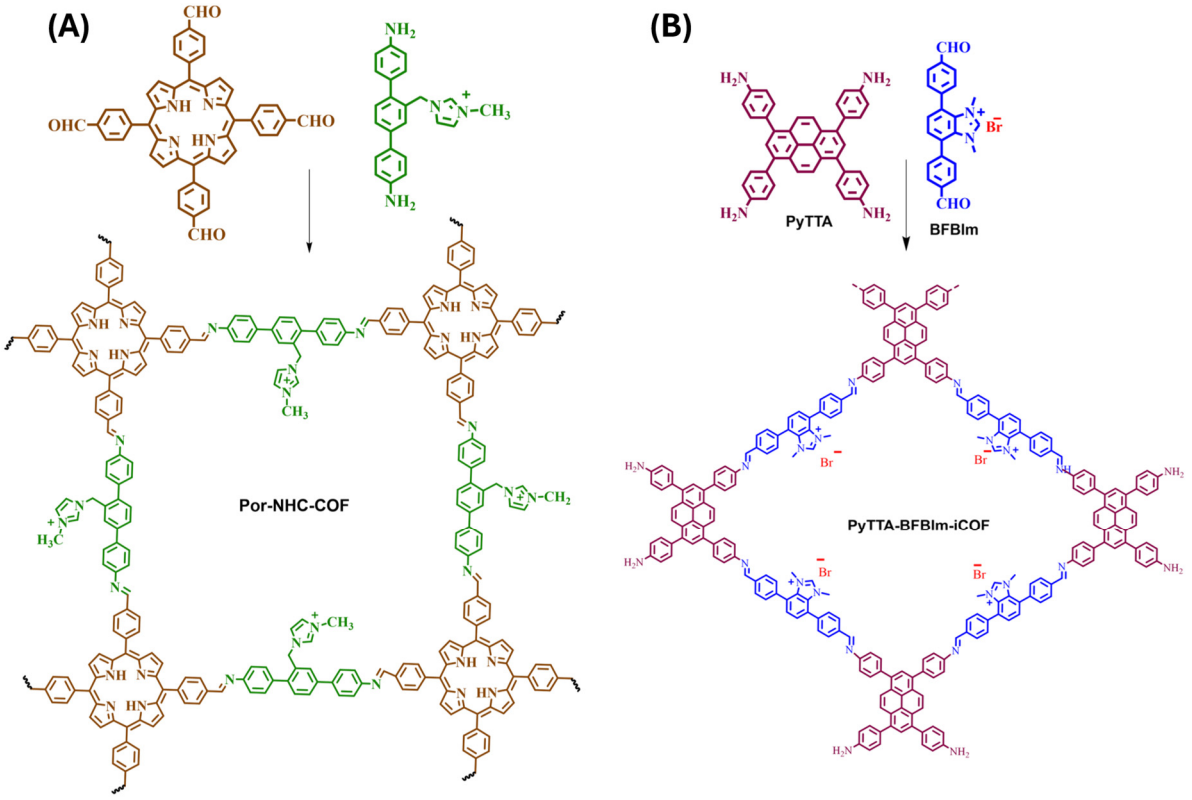


Figure 3. Synthesis of Por-NHC-COF (**A**). Synthesis of PyTTA-BFBIm-iCOF (**B**).

Huang et al. directly polymerized the cationic benzimidazolium dibromide linker BFBIm with the neutral tetraamine PyTTA in o-dichlorobenzene/n-butanol using acetic acid at 120 °C for three days, affording the imine-linked PyTTA-BFBIm-iCOF in 82% yield [29]. Its PXRD pattern contained reflections at 2θ = 3.48°, 5.14°, 7.06°, 10.60°, 14.35°, and 23.88°. Pawley refinement and structural calculations supported a reversed slipped AA-stacking model in the Pmm2 space group, with unit-cell parameters of a = 24.46 Å, b = 28.61 Å, and c = 7.44 Å. This arrangement alternately positioned the benzimidazolium groups on opposite sides of the pore walls, reducing interlayer electrostatic repulsion. Despite its ionic framework, PyTTA-BFBIm-iCOF exhibited a high BET surface area of 1532 $m^2\ g^{-1}$, a pore diameter of 2.3 nm, and a pore volume of 0.7 $cm^3\ g^{-1}$. Its PXRD pattern and accessible porosity were retained after treatment with DMF, boiling water, 3 M HCl, and 3 M NaOH. However, the material was evaluated for CO_2 adsorption and anion exchange rather than catalysis, and no free NHC or metal-NHC site was generated (Figure 3B). The corresponding PXRD patterns and structural refinements are reported in Ref. [29].

2.2. Precursor COFs and Post-Synthetic Metalation

Postsynthetic metalation reverses the order of these operations. A crystalline COF bearing imidazolium, benzimidazolium, or another masked-carbene functionality is prepared first, and the metal-NHC bond is generated only after the porous network has formed. A

single precursor COF can therefore furnish several metal derivatives, although diffusion, incomplete conversion, and the formation of non-NHC metal species become additional variables [44,48,49]. Using an ionothermal Schiff-base reaction, Yang and co-workers prepared an imine-linked precursor containing carbene and amine coordination sites and subsequently introduced palladium to obtain Pd@COF-NHC (Figure 4A). The proposed N-Pd-C environment was supported by spectroscopy, whereas microscopy and elemental mapping indicated a highly dispersed metal distribution. Nitrogen sorption showed that the BET surface area decreased from 45.6 m^2 g^{-1} for COF-NHC to 18.8 m^2 g^{-1} after Pd incorporation, corresponding to retention of about 41% of the original area. The mean pore width nevertheless remained 2.7 nm and the pore volume changed only from 0.113 to 0.106 cm^3 g^{-1}. A direct before-and-after XRD comparison was not reported; framework retention was instead inferred from nearly unchanged FT-IR and solid-state NMR spectra, an unchanged sheet-like morphology, and visible pore channels. Importantly, HRTEM lattice fringes and SAED rings also indicated crystalline Pd-containing domains, so the claim of exclusively atomically dispersed Pd-NHC sites is not fully resolved by the available characterization [31,45,59,65].

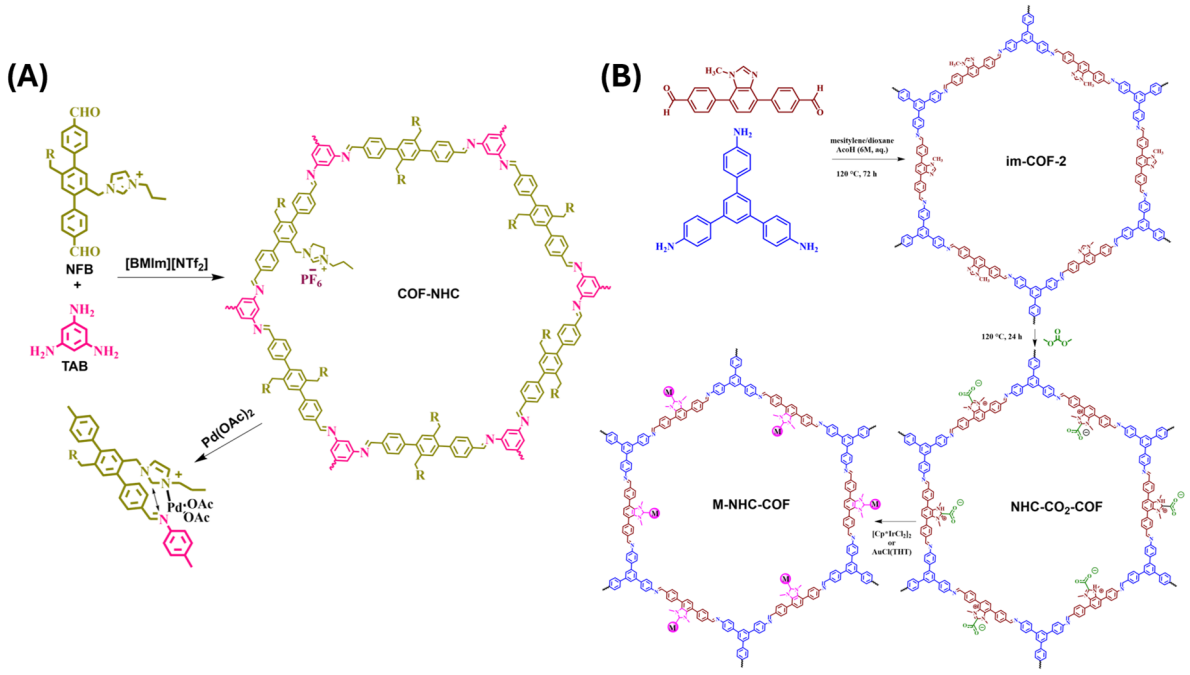


Figure 4. Synthesis of COF-NHC and Pd@COF-NHC (**A**). Synthesis of Im-COF-2, conversion to the imidazolium-carboxylate NHC-CO_2-COF, and base-free metalation with $[Cp^*IrCl_2]_2$, AuCl(THT), or $PdCl_2$ to afford M-NHC-COFs (**B**).

A milder postsynthetic strategy utilizes imidazolium carboxylates as masked carbenes. Im-COF-2 was first treated with dimethyl carbonate to form NHC-CO_2-COF and then reacted with Ir, Au or Pd precursors to form the corresponding M-NHC-COFs without a strong base or isolation of a free carbene [20]. ICP analysis gave metal loadings of 2.13 wt% Ir and 2.56 wt% Au for the corresponding derivatives. The parent Im-COF-2 exhibited PXRD reflections at $2\theta = 2.05°$, 3.48°, and 4.01°, assigned to the (100), (110), and (200) planes, respectively. Pawley refinement supported an eclipsed AA-stacking model in the P3 space group. After the two-step modification, the PXRD patterns of Ir-NHC-COF and Au-NHC-COF closely matched those of Im-COF-2, indicating that the principal long-range framework order was retained. No reflections attributable to reduced Ir or Au particles were detected, although PXRD alone cannot exclude very small clusters; the absence of metal–

metal scattering in EXAFS and the microscopy results provide stronger evidence against nanoparticle formation. Postsynthetic modification nevertheless reduced the accessible porosity. The BET surface area decreased from 932 m^2 g^{-1} for Im-COF-2 to 507 m^2 g^{-1} for Ir-NHC-COF, corresponding to retention of approximately 54% of the original area, while CO_2 uptake decreased from 32 to 26 cm^3 g^{-1} at 298 K and 1 bar. Thus, metalation largely preserved the PXRD pattern but caused a substantial loss of nitrogen-accessible surface area, consistent with occupation or partial blockage of the pores by the immobilized Ir-NHC complexes [58]. Quantitative PXRD refinements of the metalated frameworks and comparable BET values for the Au- and Pd-containing products were not reported (Figure 4B). The corresponding BET and PXRD patterns and structural refinements are reported in Ref. [20].

The masked-carbene approach was also used to prepare Pd-NHC-COF for Suzuki–Miyaura and Mizoroki–Heck coupling [38] and Ru-NHC-COF for N-H insertion followed by nucleophilic cyclization [37]. In both cases, a benzimidazolium-containing imine framework was converted into an NHC-CO_2-COF with dimethyl carbonate and then metalated. The Pd material contained 9.36 wt% metal [38], whereas the Ru material contained 7.96 wt% Ru and had a final BET area of 150 m^2 g^{-1}. Neither study reported a complete quantitative PXRD/BET comparison across the precursor, masked-carbene, and metalated states. Ordered channels were observed for Ru-NHC-COF by TEM, but this does not substitute for a before-and-after diffraction analysis. The missing structural baselines prevent a rigorous assessment of how much crystallinity or accessible porosity was lost during metalation (Figure 5A). The corresponding BET PXRD patterns and structural refinements are reported in Refs. [37,38].

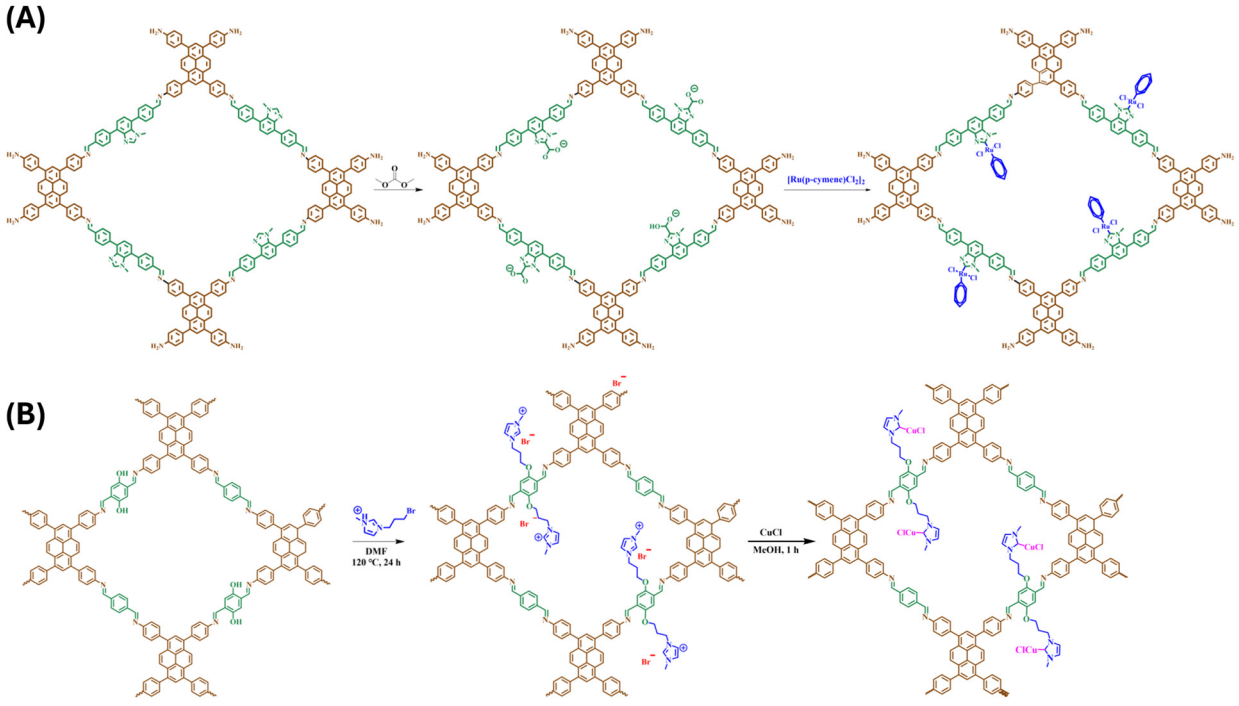


Figure 5. Synthesis of Ru-NHC-COF via two-step post-synthetic modification (**A**). Structural consequences of the stepwise post-synthetic construction of Cu(I)-NHC-COF (**B**).

A base-assisted post-synthetic route was used to prepare Cu(I)-NHC-COF [36]. PyOH-COF was first functionalized with an imidazolium ionic liquid through Williamson ether formation to produce IL-COF. The resulting material was treated with KOtBu at room temperature to generate the carbene sites and subsequently reacted with CuCl at 60 °C

under an inert atmosphere. The final material contained 5.8 wt% Cu. The characteristic PXRD reflections remained visible after ionic-liquid installation and Cu(I) incorporation, and IL-COF and Cu(I)-NHC-COF showed similar peak positions [36]. However, changes in relative peak intensity were apparent, and no Pawley refinement was performed for the modified materials. The results therefore support retention of the principal long-range framework order but do not demonstrate that crystallinity was completely unchanged. No reflections attributable to crystalline Cu-containing particles were observed, although PXRD alone cannot exclude highly dispersed or very small Cu species [45,59,65]. Post-synthetic modification caused a substantial stepwise decrease in accessible porosity. The BET surface area decreased from 2054 $m^2\ g^{-1}$ for PyOH-COF to 1197 $m^2\ g^{-1}$ for IL–COF and 838 $m^2\ g^{-1}$ for Cu(I)–NHC–COF. Thus, the final catalyst retained approximately 41% of the parent surface area. This decline was attributed to occupation and partial blockage of the pores by the bulky ionic-liquid groups and CuCl-derived sites rather than complete framework collapse. XPS supported the presence of Cu(I) and showed a new N 1 s component at 399.81 eV assigned by the authors to nitrogen associated with the carbene center (Figure 5B). The available BET and PXRD data are reported in Ref. [36].

A multistep postsynthetic strategy was used to construct the photocatalytic Cu-NHC sites [35]. The donor-acceptor pyridine framework was first exfoliated into ultrathin pCOF nanosheets, functionalized with 1-methyl-3-ethylimidazolium bromide (EmimBr), metalated with $CuCl_2$ to afford Cu(II)-im-pCOF, and subsequently reduced with ascorbic acid to produce Cu(I)-im-pCOF. The parent pCOF exhibited PXRD reflections at $2\theta = 3.0°$ and 25.5°, assigned to the (110) and (001) planes of the simulated AA-stacked structure, respectively. These peak positions remained essentially unchanged after exfoliation, imidazolium functionalization, Cu(II) incorporation, and reduction to Cu(I), indicating that the principal long-range periodicity of the framework was retained throughout the post-synthetic transformations. No diffraction peaks attributable to crystalline copper oxides were detected, although this observation alone does not establish atomic Cu dispersion; the single-site assignment was more directly supported by HAADF-STEM and the absence of a Cu-Cu scattering path in the EXAFS analysis. In contrast to the preserved PXRD features, the BET surface area decreased progressively from 872.9 $m^2\ g^{-1}$ for pCOF to 556.8 $m^2\ g^{-1}$ for im-pCOF, 251.1 $m^2\ g^{-1}$ for Cu(II)-im-pCOF, and 197.2 $m^2\ g^{-1}$ for Cu(I)-im-pCOF. The pore-size distribution nevertheless remained centered at approximately 3.0 nm. The authors attributed the surface-area loss to occupation of the internal pores by the ionic-liquid units and NHC-anchored Cu sites. Thus, this system demonstrates that retention of PXRD peak positions does not necessarily imply preservation of pore accessibility [42,58] (Figure 6A). The corresponding PXRD patterns and structural refinements are reported in Ref. [35].

A related benzimidazolium-pyrene COF was metalated with Rh and Pd precursors in the presence of potassium tert-butoxide to give Rh-NHC-COF and Pd-NHC-COF [39]. Metal loadings differed sharply, at 1.48 wt% Rh and 20.4 wt% Pd, emphasizing that precursor geometry and secondary framework coordination can govern incorporation efficiency. The precursor Im-COF had a reported BET area of 167 $m^2\ g^{-1}$, but numerical BET areas for the Rh- and Pd-metalated products and comparative PXRD data were not reported (Figure 6B) (see Ref. [39]). TEM indicated ordered architecture after metalation, yet the absence of quantitative diffraction and sorption retention values limits evaluation of structural damage.

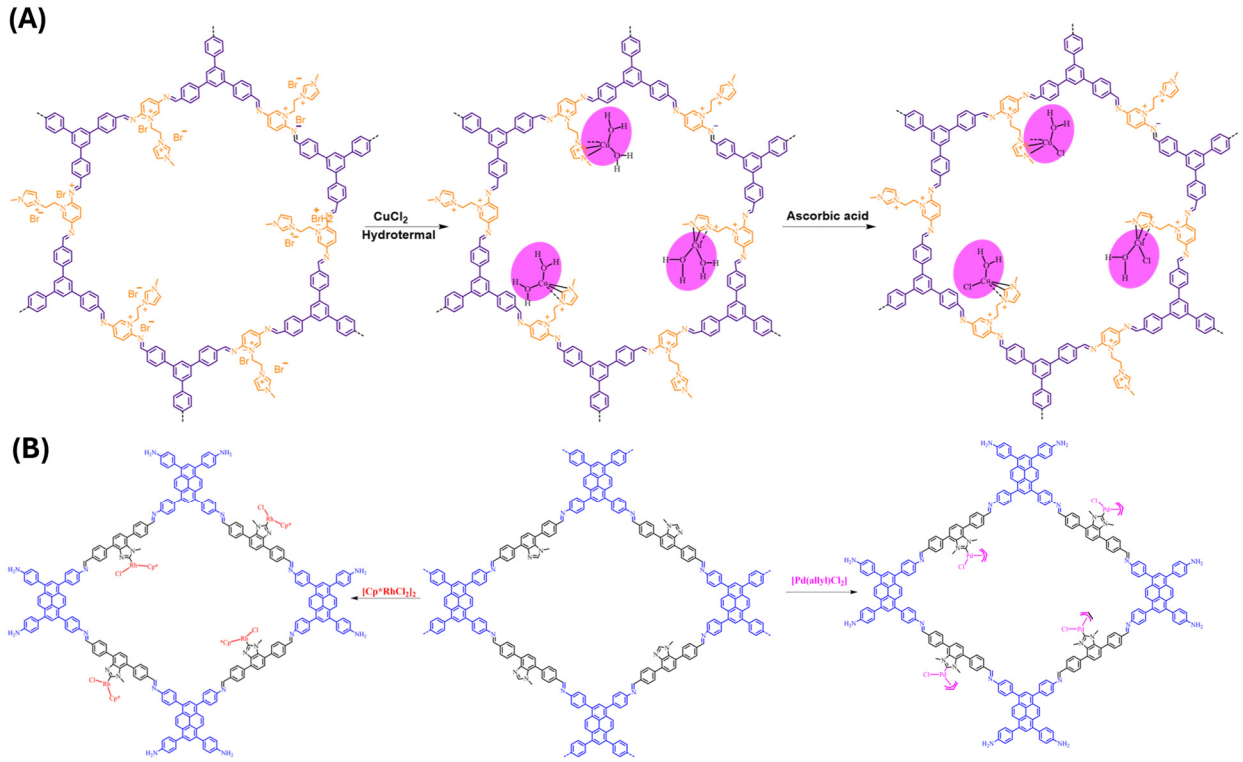


Figure 6. Structural and porosity changes during the postsynthetic construction of Cu-NHC sites in pCOF (**A**). Synthesis of the functionalized Im-COF and its Rh-NHC and Pd-NHC derivatives using $[Cp^*RhCl_2]_2$ and $[Pd(allyl)Cl]_2$, respectively (**B**).

A distinct postsynthetic strategy was used to introduce two complementary carbene-derived sites into a hydroxyl-functionalized imine COF. Preformed NHC-CuCl and NHC-CO_2 units were covalently grafted onto the pore walls through Williamson ether formation, producing COF@NHC-CuCl/CO_2 with a Cu loading of 4.23 wt%. The parent COF exhibited SAXS reflections at $2\theta = 2.8°$, 4.9°, 5.7°, and 7.5°, assigned to the (010), (110), (200), and (310) planes, respectively, and Pawley refinement supported an AA-stacked framework. Following postsynthetic functionalization, the characteristic framework reflections remained visible, although additional broad scattering developed near 20°, indicating retention of the principal periodic structure rather than a completely unchanged crystalline lattice. Consistent with the occupation of the pore channels by the two grafted functions, the BET surface area decreased from 1294.6 to 994.5 $m^2\ g^{-1}$. The two pore-size ranges also contracted slightly, from 1.1–1.6 and 2.2–3.1 nm in the parent COF to 1.1–1.5 and 2.1–2.9 nm in COF@NHC-CuCl/CO_2. Thus, the postsynthetic modification reduced accessible pore volume without eliminating the hierarchical pore network required for substrate diffusion [34]. After five catalytic cycles, however, SAXS showed retention of the (010) reflection but disappearance of the higher-order (110), (200), and (310) reflections into broad scattering features, revealing partial loss of long-range order despite preservation of catalytic activity and the imine framework. The corresponding BET patterns and structural refinements are reported in Ref. [34].

Comparison of the metal-containing systems summarized in Table 1 highlights the importance of evaluating framework order, pore accessibility, active-site identity, and post-reaction stability collectively, as illustrated in Figure 1. Retention of low-angle diffraction features may coexist with a substantial decrease in accessible surface area, as observed for Cu(I)-im-pCOF and AuNCs@NHC-COF [35,40]. Conversely, the absence of a direct parent-versus-metalated PXRD comparison, as in Pd@COF-NHC, prevents a definitive assessment of framework retention even when morphological and spectroscopic features

appear largely preserved. Accordingly, preservation of long-range order does not necessarily imply preservation of pore accessibility, while metal uptake alone does not establish the formation of a molecular M-NHC site. A credible structural assignment therefore requires convergent evidence from diffraction, gas-sorption measurements, spectroscopy, microscopy, and post-reaction characterization. Metal-free NHC, imidazolium, and ionic-precursor COFs require a related but distinct assessment and are therefore considered separately in Table 2.

Table 1. Structural and porosity changes following postsynthetic modification of metal-containing NHC-functionalized COFs and NHC-directed nanostructures.

Ref	Modification	Diffraction After PSM	BET Area Parent → Final (m^2 g^{-1})	Area Retained (%) [a]	Pore Response	Critical Assessment
[31]	COF-NHC → Pd@COF-NHC	Direct comparison not reported; crystalline Pd domains detected	45.6 → 18.8	41.2	Width retained; slight pore-volume loss	Framework retention uncertain; Pd speciation heterogeneous
[34]	Hydroxyl COF → COF@NHC-CuCl/CO_2	Main SAXS reflections retained	1294.6 → 994.5	76.8	Slight pore contraction	Good structural and porosity retention
[20]	Im-COF-2 → M-NHC-COF (Ir 2.13 wt%; Au 2.56 wt%)	Ir and Au patterns retained; no reduced-metal reflections	Ir: 932 → 507 [b]	54.4	Final pore size not reported	Crystallinity retained despite moderate area loss
[35]	pCOF → Cu(I)-im-pCOF	Peak positions retained; no Cu-oxide reflections	872.9 → 197.2	22.6 [c]	Width retained at ca. 3.0 nm	Order retained; accessible area decreased markedly
[36]	PyOH-COF → Cu(I)-NHC-COF	Main diffraction pattern retained	2054 → 838	40.8 [c]	Not reported	Framework retained with substantial pore occupation
[37]	Im-COF → Ru-NHC-COF	Comparative PXRD not reported; ordered channels seen by TEM	Not reported → 150	Not calculable	Not reported	Quantitative retention cannot be assessed
[38]	NHC-COF → Pd-NHC-COF	Not reported	Not reported	Not calculable	Not reported	Structural effects unresolved
[39]	Im-COF → Rh/Pd-NHC-COF	Comparative PXRD not reported; order inferred from TEM	167 → Not reported	Not calculable	Final pore size not reported	Quantitative retention cannot be assessed
[40]	NHC-Au(I)-COF → AuNCs@NHC-COF	Low-angle peaks retained but broadened	139 → 19.40	14.0	Main channel retained; new larger features	Severe area loss without complete framework collapse

[a] Calculated in this review as $S_{BET,\,final}/S_{BET,\,parent} \times 100$; not explicitly reported in the original articles. For multistep modifications, the value compares the final material with the initial parent COF. [b] BET values for the Au- and Pd-NHC analogues were not reported. [c] For multistep modifications, the percentage compares the final material with the initial parent COF.

2.3. Postsynthetic Activation of Metal-Free NHC and Ionic COFs

Postsynthetic modification provides a versatile route to metal-free NHC catalysis, allowing the ordered framework to be synthesized before the incorporated precursor groups are converted into catalytically active carbene sites. A representative example was reported by He et al., who addressed the air sensitivity and dimerization tendency of free NHCs by stabilizing the framework-bound carbenes as CO_2-derived carboxylate adducts [18,66,67].

Treatment of Im-COF-1 with dimethyl carbonate at 120 °C for 24 h afforded the masked-carbene material COF-NHC-CO_2 while largely preserving the framework structure. Its PXRD pattern remained consistent with that of the parent COF, whereas the BET surface area and pore volume decreased only modestly, from 817 to 761 m^2 g^{-1} and from 0.63 to 0.57 cm^3 g^{-1}, respectively. Subsequent thermal decarboxylation removed the CO_2-derived mask and regenerated isolated, catalytically accessible NHC sites within the framework. This reversible masking strategy subsequently provided the conceptual foundation for base-free carbene transfer to Ir, Au, Pd, and Ru precursors [20,37,38] (Figure 7A).

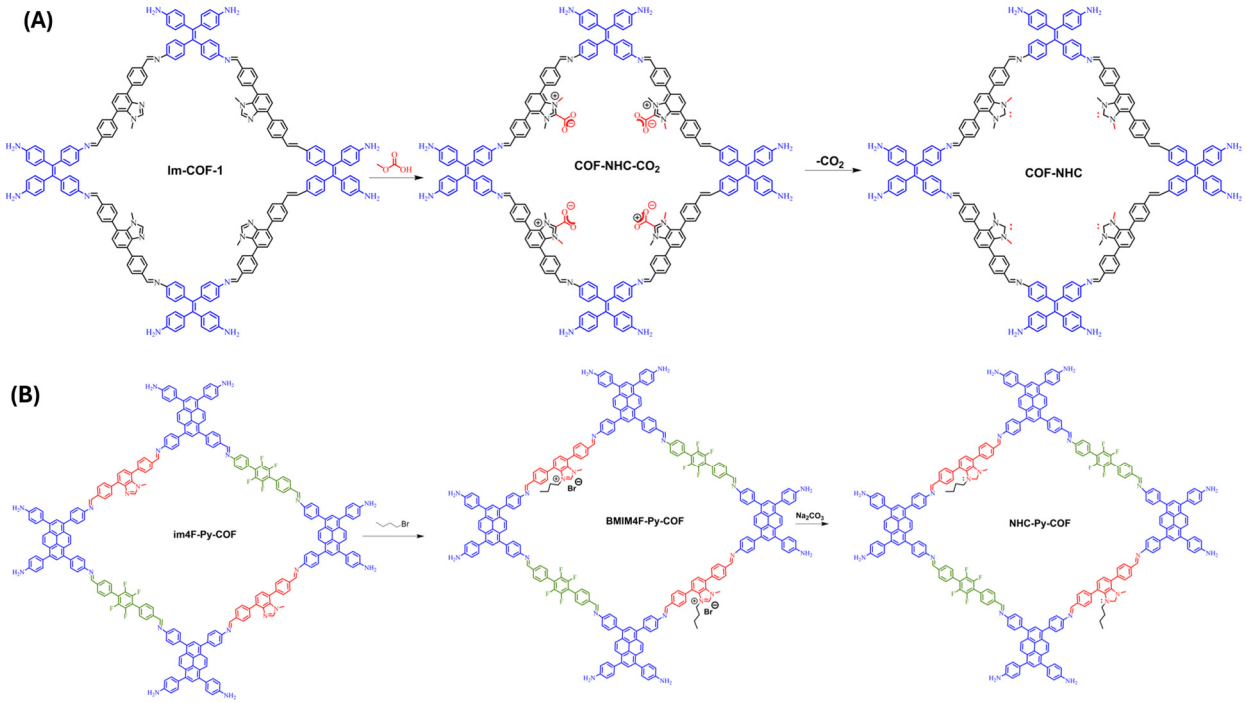


Figure 7. The post-synthetic modification of Im-COF-1 by dimethyl carbonate (DMC) to produce the CO_2-masked COF-NHC-CO_2 and its subsequent thermal decarboxylation to generate NHC-functionalized COF-NHC (**A**). Synthesis and two-step post-synthetic modification of NHC-Py-COF (**B**).

Mixed-linker benzimidazole COFs further illustrate how closely related framework architectures can generate chemically distinct catalytic sites. Chai et al. prepared IM4F-Py-COF through three-component condensation of PyTTA with equimolar benzimidazole-containing IM and fluorinated 4F dialdehydes, whereas 4F-Py-COF was synthesized separately as a benzimidazole-free control [24]. Postsynthetic quaternization of IM4F-Py-COF with 1-bromobutane afforded the ionic precursor BMIM4F-Py-COF, which was converted in situ into the catalytically active NHC-Py-COF by treatment with Na_2CO_3 during glycerol transesterification. The PXRD patterns of 4F-Py-COF, IM4F-Py-COF, and BMIM4F-Py-COF displayed similar peak positions, although the decreased diffraction intensity of the quaternized material was attributed to occupation of the pores by the grafted *n*-butyl groups. For the actual postsynthetic conversion of IM4F-Py-COF into BMIM4F-Py-COF, the BET surface area decreased from 1450 to 1326 m^2 g^{-1}, the pore width changed only slightly from 3.34 to 3.31 nm, and the pore volume decreased more markedly from 1.11 to 0.65 cm^3 g^{-1}. These results support retention of the principal framework periodicity but indicate reduced accessible pore volume following quaternization. However, because NHC-Py-COF was generated in situ and was not structurally characterized independently, preservation of the framework after carbene generation was not directly established [24] (Figure 7B).

In a related study, Yan et al. quaternized benzimidazole-containing IM4F-Py-COF with 1-bromobutane to produce BMIM4F-Py-COF for the cycloaddition of CO_2 to epoxides [25]. Unlike NHC-Py-COF, BMIM4F-Py-COF itself served as the catalyst and was not converted into a free NHC. Its PXRD pattern remained closely comparable to that of the precursor framework, whereas the BET surface area decreased from 1307 to 865 $m^2\ g^{-1}$, the pore width from 3.4 to 3.2 nm, and the pore volume only slightly from 1.09 to 1.06 $cm^3\ g^{-1}$. The authors proposed that the acidic C2-H group of the immobilized benzimidazolium cation activated the epoxide through hydrogen bonding, while Br^- promoted nucleophilic ring opening. No obvious change in the PXRD pattern was observed after five catalytic cycles. Accordingly, this material should be classified as an ionic benzimidazolium COF rather than a free-NHC or M-NHC catalyst [25].

The broader NHC-COF literature also contains useful boundary cases that should not be merged with immobilized NHC catalysis. In the conversion of imine-linked COFs to amide-linked frameworks, the NHC acts as a soluble organocatalyst for aerobic oxidation and is absent from the final material [68]. The transformation nevertheless provides a postsynthetic-modification benchmark: COFD19 to Am-COFD19 retained strong PXRD intensity with a small (100) shift from 3.20 to 3.22°, while BET area and pore width decreased from 1502 to 1137 $m^2\ g^{-1}$ and from 2.3 to 2.1 nm; COFD5 to Am-COFD5 decreased from 1755 to 812 $m^2\ g^{-1}$ and from 2.1 to 1.9 nm. The review on structural effects of post-synthetic modification [43], the NHC-dimer-linked CORN-COF [69], and NHC-protected Au nanoparticles without a COF [70] remain secondary or out-of-scope sources because they do not contain a retained framework-bound catalytic NHC or M-NHC site of the type compared here.

Table 2. Metal-free NHC-containing COFs, ionic precursors, and construction-chemistry boundary cases.

Ref	Material and Active-Site Class	Preparation or Activation	PXRD and Porosity Response	Catalytic or Functional Performance	Reuse and Heterogeneity Evidence	Review Classification
[18]	COF-NHC-CO_2; CO_2-masked carbene	Im-COF-1 + dimethyl carbonate; thermal decarboxylation generates free NHC	PXRD retained; BET 817 → 761 $m^2\ g^{-1}$	CO_2 hydrosilylation and N-formylation; >90% methanol; TOF 66.7 and 76.8 h^{-1}	At least 3 cycles; filtration stopped further reaction; PXRD, porosity, and NHC-CO_2 regeneration retained	Included metal-free organocatalyst and precursor model
[24]	NHC-Py-COF; base-generated free NHC	Mixed-linker COF → butylated BMIM4F-Py-COF; Na_2CO_3 generates NHC in situ	PXRD retained; BET 1450 → 1326 $m^2\ g^{-1}$ after butylation/the in situ generated free-NHC state was not independently characterized	Glycerol + dimethyl carbonate: 99% conversion, 96% yield; diethyl carbonate: 96%/96%	5 cycles; final conversion/yield 95%/93%; filtration or post-cycle structure not reported	Included metal-free organocatalyst
[25]	BMIM4F-Py-COF; ionic benzimidazolium bromide	IM4F-Py-COF quaternized with 1-bromobutane	PXRD retained; BET 1307 → 865 $m^2\ g^{-1}$; pore 3.4 → 3.2 nm	CO_2-epoxide cycloaddition: up to 100% yield; TON 608	5 cycles without significant loss; mid-reaction removal stopped conversion; PXRD and FT-IR retained	Included ionic catalyst; not a free NHC or M-NHC

Table 2. *Cont.*

Ref	Material and Active-Site Class	Preparation or Activation	PXRD and Porosity Response	Catalytic or Functional Performance	Reuse and Heterogeneity Evidence	Review Classification
[27]	Por-NHC-COF; imidazolium-containing metal-free COF	Direct Schiff-base polymerization; KOtBu generates NHC for lactone synthesis	Crystalline product; BET 53.0 m^2 g^{-1}	Knoevenagel: >99% yield; γ-butyrolactone: 90% yield	6 Knoevenagel cycles without significant loss; filtration stopped conversion; PXRD retained	Included metal-free bifunctional organocatalyst
[29]	PyTTA-BFBIm-iCOF; benzimidazolium precursor COF	Direct polymerization of ionic linker and neutral knot	Highly crystalline reversed slipped AA stacking; BET 1532 m^2 g^{-1}	Threefold-enhanced CO_2 uptake versus neutral analogue; anion exchange	Catalytic reuse not applicable	Precursor-design background; no M-NHC catalysis
[68]	Amide-linked COFs formed using soluble NHC	NHC-mediated aerobic oxidation of imine-linked COFs; NHC not retained	COFD19: BET 1502 → 1137; pore 2.3 → 2.1 nm; PXRD largely retained	Am-COFD19 photocatalytic dehalogenation	Catalyst-reuse evidence for an immobilized NHC site not applicable	Boundary case; final COF contains no immobilized NHC
[69]	CORN-COF; NHC-dimer-linked framework	Framework formed by NHC dimerization	Crystalline sp2-carbon-conjugated COF; comparative PSM data not applicable	Strongly reducing framework; not evaluated as an immobilized NHC catalyst in this review	Not applicable	Synthetic boundary; linkage-forming NHC is not a retained catalytic site

Comparison of the metal-free systems summarized in Table 2 reveals that retention of the principal diffraction features after masking or quaternization frequently coincides with a measurable decrease in accessible porosity. However, the chemical identity of the operating site differs substantially among these materials. Thermal decarboxylation of COF-NHC-CO_2 generates framework-bound free NHC sites [18], whereas NHC-Py-COF is produced only in situ by base treatment of its benzimidazolium precursor [24]. Consequently, the PXRD and sorption data reported for NHC-Py-COF [24] primarily characterize the precursor frameworks rather than the catalytically active free-carbene state. By contrast, BMIM4F-Py-COF functions through an immobilized benzimidazolium–bromide ion pair and should not be described as a free-NHC catalyst [25]. The directly polymerized materials [27,29] provide useful examples of metal-free NHC or ionic-site incorporation, but the absence of corresponding parent frameworks prevents quantitative assessment of structural retention. These distinctions demonstrate that the terms NHC, masked NHC, and imidazolium precursor are not interchangeable and must be assigned according to the active species supported by the available evidence.

2.4. Dual Sites and Spatially Programmed Functions

The most distinctive M-NHC-COFs use the framework to place complementary functions within the same pore system. This principle is illustrated by a hydroxylated COF bearing both NHC-CuCl and NHC-CO_2 groups [34]. The Cu(I) site was proposed to activate the alkyne as a soft Lewis acid, whereas the NHC-CO_2 adduct supplied a bent, polarized CO_2 unit. The combined control experiments and calculations therefore support a cooperative two-site model, although the exact spatial arrangement of the sites during turnover was not directly observed. The final material contained 4.23 wt% Cu, while its BET surface area decreased from 1294.6 to 994.5 m^2 g^{-1} after functionalization, indicating substantial retention of accessible porosity despite installation of both catalytic functions. The chiral NHC-Au-SA-COF follows the same architectural principle in a sequential re-

action [33]. Au-NHC sites oxidize aryl methanols, and chiral secondary amines catalyze the ensuing asymmetric aldol reaction. The framework integrates both functions, but the original study did not directly resolve the distance between the two operating sites [71–74].

2.5. NHC Stabilized Nanoparticles and Nanoclusters

The two immobilization routes also produced distinguishable structural and porosity responses. The parent TPT-PDA COF exhibited PXRD reflections at $2\theta = 2.7°$, 4.7°, 5.4°, and 7.2°, assigned to the (100), (110), (200), and (210) planes, respectively [22]. Following incorporation and reduction of the NHC-Au(I) precursor, the hybrid materials retained recognizable low-angle COF reflections and developed additional peaks at 38.2° and 44.4°, corresponding to the (111) and (200) planes of crystalline metallic Au. These high-angle reflections confirm that the final materials contain Au nanoparticles rather than exclusively molecular Au–NHC sites [60]. The BET surface area decreased from 1885 $m^2\ g^{-1}$ for TPT–PDA COF to 1106 and 910 $m^2\ g^{-1}$ for NHC@AuNP-1@COF and NHC@AuNP-2@COF, respectively. Their corresponding pore widths were 2.88, 2.35, and 2.51 nm. After five catalytic cycles, the PXRD pattern of NHC@AuNP-1@COF remained similar to that of the fresh catalyst, and the Au(111) and Au(200) reflections remained observable, indicating persistence of the crystalline Au nanoparticles and the principal framework structure [22] (Figure 8A). Reduction of the framework-bound Au(I) precursor produced a more pronounced structural and porosity change in AuNCs@NHC-COF [40]. The reduced composite retained reflections at $2\theta = 2.0°$, 3.2°, and 4.1°, corresponding to the (100), (110), and (200) planes of the parent NHC-Au(I)-COF. However, the broadening of the (100) reflection at 2.0° was attributed to the formation of nanoclusters which resulted in lattice imperfections and microstrain. The BET surface area decreased significantly from 139 $m^2\ g^{-1}$ for NHC-Au(I)-COF to 19.40 $m^2\ g^{-1}$ for AuNCs@NHC-COF, indicating significant occupation or blockage of the accessible pore space. PXRD alone could not establish the size and dispersion of the Au nanoclusters and TEM, HRTEM and SAED confirmed their mean diameter of 1.66 ± 0.09 nm and metallic lattice structure. After four photocatalytic cycles, the PXRD pattern remained largely preserved but showed a slight decrease in crystallinity, while TEM revealed no obvious AuNC aggregation [40] (Figure 8B).

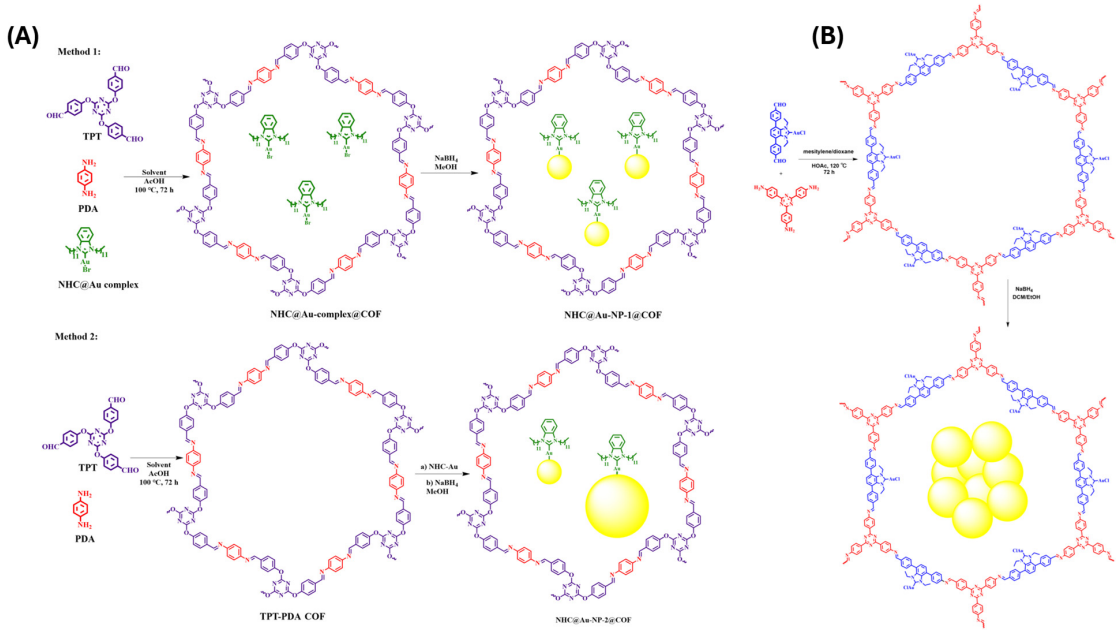


Figure 8. Preparation of COF-immobilized gold NPs with two methods (**A**). Synthesis route of AuNCs@NHC-COF (**B**).

3. Catalytic Applications

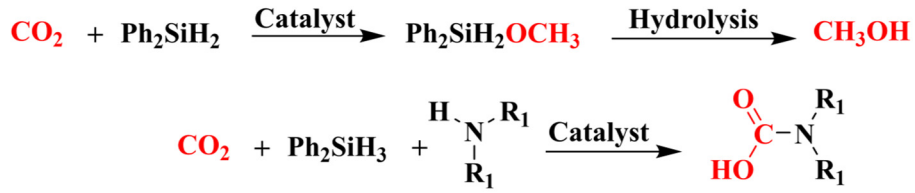
Catalytic applications of NHC-functionalized COFs span metal-free organocatalysis, ionic-site catalysis, molecular M-NHC catalysis, and NHC-directed metallic particles. These classes are organized below by transformation rather than ranked together, because their active-site chemistry and test conditions are not equivalent. For each material, the framework architecture and active-site assignment are introduced before the corresponding reaction and mechanism. Structural changes caused by postsynthetic modification are not repeated here; the relevant PXRD and BET comparisons are consolidated in Section 2 and Tables 1 and 2.

3.1. CO_2 Utilization

CO_2 utilization through organocatalytic, ionic, and metal-mediated pathways requires distinct modes of substrate and CO_2 activation. NHCs may activate silanes nucleophilically, stabilize CO_2-derived zwitterionic species, or electronically modify metal centers responsible for carboxylation and hydrogenation [50,75,76].

3.1.1. Metal-Free CO_2 Hydrosilylation and N-Formylation

A reversible CO_2 mask enabled a stable imidazolium carboxylate to function as the precursor to an immobilized free carbene. Heating COF-NHC-CO_2 released the bound CO_2 and exposed spatially separated NHC sites without adding a strong base [18]. The neutral Im-COF-1 precursor, dimethyl carbonate, and the absence of catalyst were ineffective controls, whereas a physical mixture of the molecular NHC-CO_2 analogue and Im-COF-1 remained less active than the covalently integrated material. The authors attributed this difference to suppression of inactive NHC dimerization and ordered dispersion of the carbene sites within the pores (Figure 7A). Under 0.1 MPa CO_2 at 60 °C in DMF, COF-NHC-CO_2 completely consumed diphenylsilane within 6 h; hydrolysis of the methoxysilanes afforded methanol in greater than 90% yield, with a reported TOF of 66.7 h^{-1}. The same material catalyzed N-formylation of amines with CO_2 and phenylsilane with a TOF of up to 76.8 h^{-1}. $^{13}CO_2$ labeling confirmed incorporation of external CO_2 into methanol and N-formylmorpholine, while detection of some ^{12}C product showed that the framework-bound CO_2 mask was also released and entered the reaction pool (Scheme 2).



Scheme 2. Metal-free CO_2 hydrosilylation and N-formylation by thermally generated NHC sites in COF-NHC-CO_2.

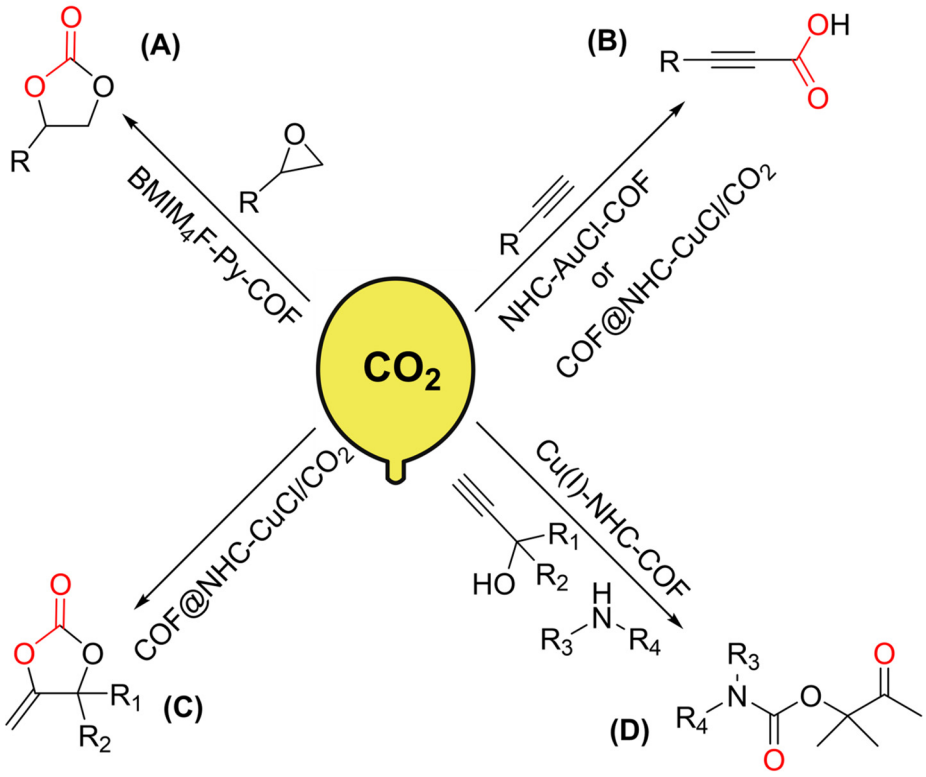
DFT calculations and in situ infrared spectroscopy supported silane-first activation. NHC attack on diphenylsilane to form a silane-NHC adduct had a calculated activation energy of 22.2 kcal mol^{-1}, compared with 32.6 kcal mol^{-1} for the pathway in which CO_2 first formed the NHC-CO_2 intermediate [18]. The calculations therefore support preferential nucleophilic activation of the silane, although the complete cycle remains partly computational. Filtration after 3 h stopped further product formation, and the catalyst was reused at least three times without loss of activity or selectivity. PXRD, nitrogen sorption, and solid-state ^{13}C NMR of the recovered solid indicated retention of porosity and regeneration of the NHC-CO_2 protecting group [77].

3.1.2. Ionic CO_2-Epoxide Cycloaddition

BMIM4F-Py-COF represents an ionic catalytic pathway rather than free-carbene or metal-carbene chemistry. Quaternization of the benzimidazole-containing IM4F-Py-COF with 1-bromobutane positions benzimidazolium bromide pairs along the one-dimensional channels [25]. The retained C2-H group and bromide counterion provide complementary electrophilic and nucleophilic functions, while the porous framework prevents loss of the ionic liquid and permits recovery of the solid [78,79] (Figure 7B).

In the solvent- and cocatalyst-free model reaction, epichlorohydrin and CO_2 at 4.0 MPa and 110 °C afforded the cyclic carbonate in 97% yield after 12 h. Across the reported substrate set, yields reached 100% and the maximum TON was 608. Lower temperature, pressure, catalyst amount, or reaction time reduced conversion, showing that the ionic catalyst remained dependent on relatively demanding CO_2 pressure and heating despite avoiding solvent and an added cocatalyst.

The authors propose that the benzimidazolium C2-H group hydrogen bonds to the epoxide oxygen and weakens a C-O bond; bromide then attacks the less hindered carbon, followed by CO_2 insertion into the alkoxide and ring closure to the cyclic carbonate [25]. This pathway is chemically reasonable but was not established by detection of catalytic intermediates or computation. Removal of the solid during reaction stopped conversion, and activity was retained through five cycles with preserved PXRD and FT-IR patterns (Scheme 3A).



Scheme 3. CO_2-utilization pathways in NHC-functionalized COFs: ionic CO_2-epoxide cycloaddition over BMIM4F-Py-COF (**A**); Au-NHC-catalyzed alkyne carboxylation (**B**); cooperative CO_2 fixation by the dual-site NHC-CuCl/NHC-CO_2 catalyst (**C**); and CO_2-fixation reactions catalyzed by Cu(I)-NHC-COF (**D**).

3.1.3. Carboxylative Coupling and Alkyne Carboxylation

Direct incorporation of an Au(I)-NHC monomer provided one of the earliest routes to a COF catalyst for CO_2 utilization. Li and co-workers condensed a preformed Au(I)-NHC

dialdehyde with a triamine to generate an imine-linked NHC-AuCl-COF (Figure 2A) [32]. Because metallation preceded polymerization, diffusion through an already formed pore was not required and the Au-NHC unit was distributed as part of the framework backbone. Subsequent anion exchange afforded NHC-AuSbF6-COF without rebuilding the network, allowing counterion effects to be examined within the same COF architecture. The structural characterization of this directly polymerized material is discussed in Section 2.1.

Catalytic evaluation first focused on direct carboxylation of terminal alkynes with CO_2 (Scheme 3B). Under 1 atm CO_2, NHC-AuCl-COF converted phenylacetylene in DMSO or DMF at 50 °C with 0.5 mol% Au and Cs_2CO_3, affording the propiolic acid in 96% isolated yield after 16 h. These data correspond to a TON of 192 and a TOF of 12 h^{-1}. Electron-rich and electron-poor arylacetylenes generally gave 95–99% yields, whereas a hydroxy-substituted substrate and an aliphatic alkyne produced almost no desired carboxylation product, revealing a substrate-dependent limitation. The recovered catalyst still afforded 94% yield in the fifth cycle; PXRD and XPS indicated retention of the framework and Au(I) state, and ICP analysis showed approximately 1% Au loss. Counterion exchange generated a second catalytic function: NHC–$AuSbF_6$–COF hydrated phenylacetylene in water at 60 °C in 99% yield after 20 h, compared with 20% for NHC-AuCl-COF under the same conditions. The water contact angle decreased from 123 ± 2° to 0°, correlating the improved aqueous-phase reactivity with increased wettability, although a simultaneous electronic effect of SbF_6^- on Au cannot be excluded. The hydration catalyst retained 94% yield after five cycles without a measurable change in Au content or oxidation state [32] (Scheme 3B).

Whereas the Au material relies on a single metal site, the Cu system reported by Guo and co-workers was designed to activate both reaction partners independently [34,80]. Post-synthetic grafting generated NHC-CuCl sites together with NHC-CO_2 adducts in the same hydroxylated framework. The Cu(I) center was assigned the role of coordinating the alkyne or propargylic substrate, while the carbene-CO_2 adduct supplied a preorganized, polarized carbon dioxide molecule. The final material contained 4.23 wt% Cu; the accompanying SAXS, BET, and pore-size changes are reported in Section 2.2 and Table 1.

Under atmospheric CO_2, the bifunctional material catalyzed cyclization of propargylic alcohols to α-alkylidene cyclic carbonates, reaching space–time yields of 71.9 h^{-1} at 40 °C and 36.7 h^{-1} at 25 °C. Several substituted alcohols afforded more than 90% yield under the optimized conditions. The same catalyst also converted terminal alkynes into propiolic acids in 73–92% yield at 40 °C, demonstrating that the cooperative arrangement was not restricted to one substrate class (Scheme 3B,C).

Experiments and density functional theory calculations support a cooperative two-site model. NHC-CO_2 bends the O-C-O unit to 132.7° and lengthens both C-O bonds, making the bound carbon dioxide more reactive than linear CO_2. For propargylic-alcohol coupling, the calculated CO_2-insertion barrier fell from 35.9 kcal mol^{-1} for free CO_2 to 17.4 kcal mol^{-1} for the NHC-CO_2 pathway. For terminal-alkyne carboxylation, the corresponding barrier decreased from 50.8 to 30.2 kcal mol^{-1}. Hot-filtration and ICP analyses detected no Cu in the filtrate, and yields remained above 92% through five cycles. The (010) reflection was retained after reuse, whereas several higher-order reflections disappeared; catalytic stability should therefore not be equated with complete preservation of long-range crystallographic order. These results support a cooperative benefit, although the exact turnover-site geometry remains modeled rather than directly observed.

A second Cu catalyst simplified the architecture by using one principal metal-NHC function. Parihar and co-workers first grafted an imidazolium ionic-liquid unit onto a pyrene-based hydroxyl COF and then treated the material with potassium tert-butoxide and CuCl to form Cu(I)-NHC-COF (Figure 5B). The use of a strong base distinguishes this

route from the masked-carbene metalations discussed below. Its diffraction and porosity changes are compared in Section 2.2 and Table 1.

In the presence of DBU and DMF, Cu(I)-NHC-COF converted a propargylic alcohol under 1 atm CO_2 into the corresponding α-alkylidene cyclic carbonate with more than 99% conversion and 100% selectivity at 50 °C in 9 h. At 25 °C, only 22% conversion was obtained after 3 h; thus, atmospheric pressure should not be conflated with fully ambient operation. Addition of a secondary amine furnished β-oxopropylcarbamates in more than 99% yield and 100% selectivity at 50 °C over 12 h. Control reactions identified the cyclic carbonate as the intermediate in this three-component process, followed by amine addition and tautomerization (Scheme 3C,D).

The material also operated with simulated dry flue gas containing 13% CO_2, giving 52% conversion after 9 h and 99% after 18 h. It was recycled ten times with only a small decline, and the filtrate contained 0.08 ppm Cu. The study therefore adds two practically relevant features to the field: dilute-gas operation and extended reuse. Its use of DMF and an added base, however, shows that mild pressure and temperature do not alone establish a green process.

3.1.4. CO_2 Hydrogenation to Formate

Among the postsynthetic strategies [81], the masked-carbene route of He and co-workers provides the most direct response to the instability of free NHCs [20]. An imine-linked COF containing NHC-CO_2 groups was heated with a Cp*Ir precursor, causing decarboxylative carbene transfer without an external base or isolation of the free carbene. X-ray absorption spectroscopy supported an isolated Ir-NHC coordination environment and showed no Ir-Ir scattering, providing strong local-structure evidence against particle formation. The PXRD, BET, and CO_2-uptake changes associated with metalation are discussed in Section 2.2 and Table 1.

The supported Ir complex catalyzed hydrogenation of CO_2 to formate at 120 °C under a total CO_2/H_2 pressure of 8 MPa (Figure 4B). An initial TOF of 17,244 h^{-1} was reported, and the formate concentration reached 0.42 M, corresponding to a TON of 27,015 after 15 h. Neither Im-COF-2 nor NHC-CO_2-COF produced formate, while homogeneous $[Cp^*IrCl_2]_2$ and its physical mixture with Im-COF-2 were less active. These controls support a specific contribution from the framework-bound Ir-NHC environment, although they do not isolate confinement from every other difference in coordination and dispersion. The initial TOF and final TON were measured at different reaction times and therefore describe different aspects of catalyst performance. The requirement for 8 MPa total gas pressure remains a substantial process limitation.

Spectroscopy and calculations connected the activity to the electronic effect of the carbene. NHC coordination made Ir more electron-rich, increased the calculated CO_2 adsorption energy from 7.1 to 8.4 kcal mol^{-1} relative to the homogeneous precursor, and lowered the barrier for CO_2 insertion into an Ir-H intermediate by 2.8 kcal mol^{-1}. The catalyst was recovered by centrifugation and reused five times without a measurable loss in activity. Its BET surface area after recovery was 483 m^2 g^{-1}, close to the fresh value of 507 m^2 g^{-1}, and microscopy found no Ir aggregation. These results provide strong evidence for retention of isolated Ir sites after catalysis, although operando identification of the turnover-state coordination environment was not reported.

3.2. Carbon–Carbon Bond Formation

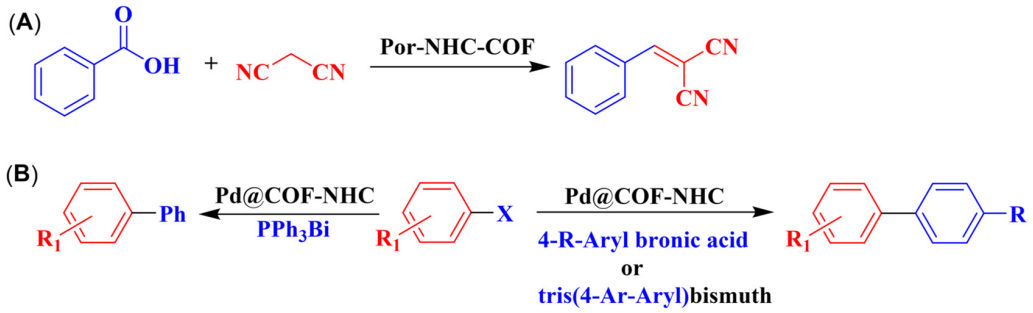
Carbon–carbon bond formation illustrates the breadth of the catalyst classes especially clearly. Por-NHC-COF promotes a base-type condensation without a metal, whereas Pd-NHC-COFs perform oxidative-addition and transmetalation chemistry. Their yields should

therefore be evaluated within each mechanistic family rather than compared as if they represented interchangeable catalysts [82–85].

3.2.1. Metal-Free Knoevenagel Condensation

Por-NHC-COF was constructed directly from an imidazolium-containing diamine and a porphyrin aldehyde, placing imidazolium, imine, and porphyrinic N-H functions within the same metal-free framework [27] (Figure 3A). The authors assigned the Knoevenagel activity primarily to the basic environment created by the imine and pyrrolic N-H sites, with the positively charged imidazolium unit proposed to polarize the aldehyde through electrostatic interaction. The material should therefore be described as a bifunctional ionic/basic COF rather than assuming that a free NHC is present under the base-free Knoevenagel conditions.

Condensation of 4-nitrobenzaldehyde with malononitrile in toluene-water containing 25% water reached greater than 99% yield at room temperature within 1 h. The uncatalyzed reaction and the isolated monomers gave only 24–30% yield under the comparison conditions. Substituted benzaldehydes afforded 53–99% yield, with electron-withdrawing groups generally reacting more efficiently than electron-donating groups. Removing the solid after 30 min stopped further product formation, and the catalyst was reused for six runs without significant activity loss; the PXRD pattern remained intact after cycling (Scheme 4A).



Scheme 4. Carbon–carbon bond formation: metal-free Knoevenagel condensation within the multifunctional Por-NHC-COF pore (**A**). C-C coupling reactions catalyzed by Pd@COF-NHC COFs (**B**).

3.2.2. Pd-NHC-Catalyzed Cross-Coupling

Pd-NHC-COFs constitute the most developed subgroup for carbon–carbon bond formation, but the three available studies differ markedly in solvent, temperature, Pd loading, and evidence for site nuclearity. The comparison is therefore most informative when construction, reaction performance, and heterogeneity tests are considered together [86–88].

The first Pd platform was obtained from an NHC-containing imine COF whose coordination sites were treated with $Pd(OAc)_2$ (Figure 4A) [31]. Yang and co-workers assigned the incorporated palladium to a proposed N–Pd–C environment based on XPS and solid-state NMR, and elemental mapping showed a highly dispersed distribution. The 20.1 wt% Pd loading was close to the theoretical value. HRTEM and SAED nevertheless indicated crystalline Pd-containing domains, so the nuclearity of all active Pd species cannot be assigned unambiguously. The BET, pore-volume, and diffraction limitations of this postsynthetic metalation are summarized in Section 2.2 and Table 1.

Pd@COF-NHC coupled aryl halides with arylboronic acids in water at room temperature [31]. Under the representative conditions, aryl halide (0.50 mmol), arylboronic acid (0.55 mmol), K_2CO_3 (1.5 mmol), 0.5 mol% Pd, and 2.5 mL H_2O, the Suzuki–Miyaura reaction reached 99% isolated yield within 1 h, and electron-withdrawing and electron-donating substituents were tolerated. The catalyst was reused for at least eight cycles without a significant activity loss. Hot filtration essentially arrested further conversion: after removal of the

solid catalyst at 46.9% yield, the filtrate reached only 47.5% and 48.6% after an additional 1 and 4 h, respectively. Palladium in the filtrate was below 1 ppm, corresponding to less than 0.05% of the initial Pd inventory. TEM showed no evident morphological change or Pd aggregation after recycling, and XPS indicated retention of the palladium species; however, post-cycle PXRD and BET data were not reported. The same material coupled aryl iodides with triarylbismuth reagents using 2 mol% Pd and K_2CO_3 in EtOH/H_2O (4:1) at room temperature, giving 96% yield for the model reaction after 5 h. These conditions were substantially milder than those reported for the earlier Pd-COF systems cited in the original study, although the high Pd content and unresolved contribution of crystalline Pd-containing domains complicate assignment of the molecular active site (Scheme 4B).

A second palladium platform was prepared through benzimidazolium-derived masked-carbene metalation [38]. Under the optimized Suzuki–Miyaura conditions, 3 mg catalyst, 0.30 mmol aryl halide, 0.45 mmol arylboronic acid, 2 equiv K_2CO_3, and 3 mL DMF at 120 °C for 24 h in air, the model aryl-bromide product was obtained in 92% yield, while the corresponding aryl iodide substrate gave 93% yield. A 3 mmol experiment afforded 85% yield, providing a limited indication of preparative scalability. The same material promoted Mizoroki–Heck coupling with high *Z*/*E* selectivity and retained activity over five cycles. Quantitative leaching data and post-cycle PXRD or porosity measurements were not reported; consequently, recycling alone does not establish retention of a molecular Pd-NHC site. Its higher temperature and use of DMF are also less favorable than the aqueous room-temperature conditions reported for Pd@COF-NHC, although the catalysts were not tested under equivalent conditions and their yields do not constitute a direct activity ranking (Scheme 4B, right).

Metalation of a benzimidazolium-bearing pyrene COF produced a third Pd material with a loading of 20.4 wt% [39] (Figure 6B). Spectroscopic measurements supported Pd binding to the carbene-containing framework, whereas microscopy showed an ordered sheet-like architecture together with granular high-contrast regions. Pd(0) domains or nanoparticles could therefore coexist with nominal molecular Pd-NHC sites. This distinction is important because high metal uptake increases apparent site density but can also promote metallic ensembles. The unavailable post-metalation PXRD and BET comparisons are noted in Section 2.2 and Table 1.

With this high-loading catalyst, representative Suzuki–Miyaura and Mizoroki–Heck reactions used 3 mg catalyst, 2 equiv KOtBu, and 3 mL i-PrOH at 60 °C for 12 h. When the solid was removed during a coupling experiment, the yield remained at 34%, and the filtrate contained less than 5 ppm Pd. The bulk Pd content changed only from 20.4 to 19.8 wt% after cycling. These measurements argue against sustained catalysis by a large pool of dissolved Pd, but they do not exclude transient leaching–redeposition or distinguish isolated Pd-NHC centers from small clusters or Pd(0) domains under the strongly basic reaction conditions (Scheme 4B, right).

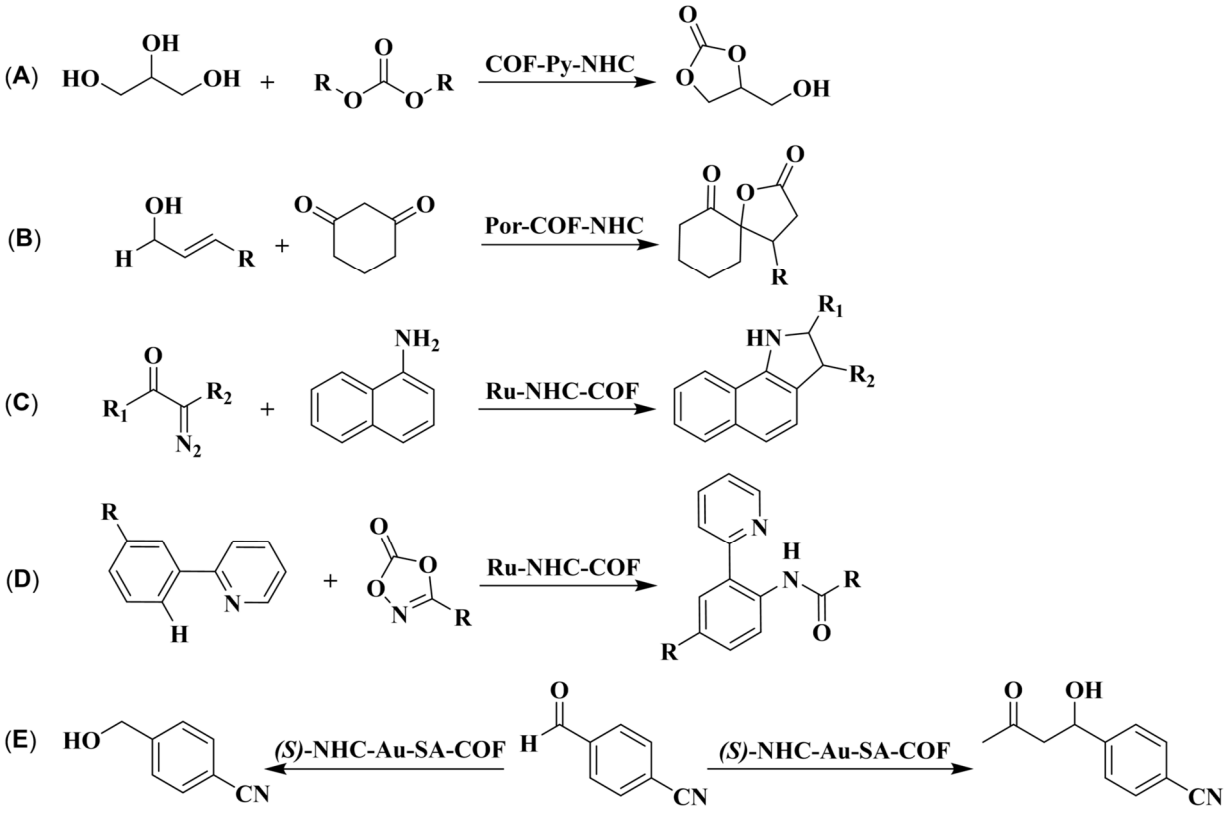
Together, the three Pd studies establish a progression from room-temperature aqueous coupling, through modular NHC-CO_2 transfer chemistry, to high-loading pyrene frameworks with a lower operating temperature than the immediate predecessor. They also reveal a persistent analytical problem. Palladium readily changes oxidation state during cross-coupling, and the active species may evolve between molecular, cluster, and nanoparticle forms. Operando X-ray absorption or pair-distribution analysis would provide stronger evidence than post-reaction characterization alone.

3.3. Other Metal-Free NHC-Catalyzed Transformations

3.3.1. Glycerol Transesterification

The mixed-linker NHC-Py-COF was generated by incorporating benzimidazole groups into a pyrene COF, quaternizing them with 1-bromobutane, and adding sodium carbonate to deprotonate the resulting benzimidazolium sites in situ [24] (Figure 7B). Control experiments with the neutral COFs and with BMIMBr did not produce the transesterification product, whereas the framework-generated carbene was active. This comparison supports free NHC formation as the operative step, although the carbene itself was not isolated or directly quantified.

With 5 mol% NHC-Py-COF generated using 2.5 mol% sodium carbonate, glycerol and dimethyl carbonate reacted at 70 °C for 8 h to give 99% conversion and 96% yield [24]. For diethyl carbonate, 96% conversion and 96% yield were obtained. The fifth reuse achieved 95% conversion and 93% yield, slightly lower than the first cycle. The study did not report a filtration experiment or post-cycle structural characterization, so recyclability alone does not fully establish retention of the carbene state or framework integrity. The authors propose nucleophilic acyl substitution initiated by the attack of the framework NHC on dimethyl carbonate. Methoxide released from this intermediate deprotonates glycerol, and successive alkoxide attack, methoxide departure, and intramolecular carbonate formation regenerate the carbene [24]. Because no intermediate was detected and no computational profile was reported, the cycle should be presented as proposed rather than proven (Scheme 5A).



Scheme 5. Catalytic transformations involving metal-free and molecular M-NHC sites: NHC-catalyzed glycerol transesterification with dimethyl carbonate (**A**); γ-butyrolactone formation over Por-NHC-COF (**B**); Ru-NHC-catalyzed N-H insertion and nucleophilic cyclization (**C**); Rh-NHC-catalyzed directed C-H amidation (**D**); and sequential Au-NHC oxidation and chiral-amine aldol catalysis within a single COF (**E**).

3.3.2. γ-Butyrolactone Synthesis

The directly polymerized Por-NHC-COF introduced in Section 3.2.1 displayed a second catalytic mode after treatment with potassium tert-butoxide [27] (Figure 3A). Under these strongly basic conditions, deprotonation of the imidazolium unit was proposed to generate the active carbene; the need for strong base and the absence of product without the COF are consistent with this assignment, but direct spectroscopic observation of the carbene was not reported.

Reaction of 1,2-cyclohexanedione with cinnamaldehyde in THF at room temperature, using 0.22 mol% Por-NHC-COF and potassium tert-butoxide, afforded the γ-butyrolactone product in 90% isolated yield after 12 h. The reported cinnamaldehyde derivatives generally gave yields above 80%. The authors proposed that addition of the NHC to the enal forms a homoenolate, which reacts with the diketone through addition and cyclization before releasing the catalyst. This mechanism was inferred from established NHC chemistry rather than supported by detected intermediates or DFT calculations (Scheme 5B).

These two studies illustrate different compromises in metal-free NHC catalysis. NHC-Py-COF approaches the activity of a homogeneous NHC analogue but requires added carbonate base and lacks post-cycle structural analysis [24]. Por-NHC-COF operates at room temperature and at low nominal catalyst loading for lactone synthesis, but it relies on potassium tert-butoxide and does not directly establish the concentration of generated carbene sites [27]. Future comparisons should quantify accessible NHC density and report TON on that basis rather than on total framework mass or nominal monomer content.

3.4. C-H and N-H Functionalization

Extension beyond classical cross-coupling introduced reactions in which the supported metal must generate short-lived carbene or nitrene intermediates. In these systems, immobilization is valuable only if the coordination environment remains sufficiently labile for substrate binding while preventing irreversible aggregation [44,89–93].

For N-H insertion chemistry, a benzimidazolium-derived COF bearing NHC-CO_2 groups was subjected to decarboxylative carbene transfer with a Ru precursor [37] (Figure 5A). The resulting Ru-NHC-COF contained 7.96 wt% Ru. The procedure avoided isolation of a free NHC and generated a supported site designed to form a cationic Ru-carbene intermediate after halide abstraction. The incomplete PXRD and BET comparison across the precursor, masked-carbene intermediate, and Ru product is discussed in Section 2.2 and Table 1.

Reaction of naphthylamines with diazo esters in the presence of Ru-NHC-COF produced benzoindoles through N-H insertion followed by intramolecular nucleophilic cyclization [37]. Using 3 mg of catalyst and 15 mol% $AgSbF_6$ in DCE at 100 °C for 12 h under an Ar atmosphere, the model product was isolated in 78% yield; by comparison, $AgNTf_2$ afforded 37% yield under otherwise comparable conditions. Electron-rich and electron-poor naphthylamines and several diazo esters were tolerated, while a 2 mmol experiment also gave 78% yield. The recovered catalyst was reused over five cycles, but quantitative metal leaching and post-cycle structural analyses were not reported (Scheme 5C).

The proposed sequence begins with halide abstraction and formation of a cationic Ru carbene, followed by amine insertion into the Ru-bound carbene. The resulting N-H insertion product undergoes intramolecular attack, rearrangement, and dehydration to form the benzoindole. High-resolution mass spectrometry detected an N-H insertion intermediate. Calculations also found more favorable binding and migratory-insertion energetics for Ru-NHC-COF than for the homogeneous ruthenium precursor. The need for a silver salt and chlorinated solvent tempers the sustainability claim, but the reaction expands COF-supported NHC catalysis into cascade heterocycle synthesis.

The pyrene-based NHC precursor used for Pd coupling also accommodated a Cp*Rh fragment, yielding a framework-bound Rh-NHC environment with 1.48 wt% Rh (Figure 6B). Installing a different metal on the same general platform redirected the chemistry from cross-coupling to Rh(III)-mediated C-H activation and nitrene transfer. The large difference between Rh and Pd loadings further shows that incorporation efficiency depends strongly on precursor geometry and secondary interactions with the framework. The unavailable post-metalation PXRD and BET data are identified in Section 2.2 and Table 1.

For directed C-H amidation, Rh-NHC-COF reacted the arene substrate with 1.5 equiv dioxazolone using 3 mg catalyst and 15 mol% $AgNTf_2$ in 2 mL DCE at 100 °C for 24 h, affording the model amide in 82% yield [39]. The catalyst was reused for five cycles. The authors proposed a Rh(III)-mediated sequence involving directed C-H activation, nitrene transfer, and protonation; DFT gave a 19.8 kcal mol^{-1} barrier for C-H activation. Because no operando Rh intermediate was detected, the cycle should be regarded as computationally supported rather than experimentally proven (Scheme 5D).

The proposed Rh(III) cycle includes directed C-H activation, dioxazolone coordination, migratory insertion with CO_2 loss, and protonation. The calculated barrier for C-H activation was 19.8 kcal mol^{-1} and was lower than that of the homogeneous $[Cp^*RhCl_2]_2$ reference. As in the Ru system, a silver salt was required to generate the cationic active species. The two studies show that M-NHC-COFs can support bond activation and carbene or nitrene transfer, but additive-free variants remain an important target.

3.5. Asymmetric and Relay Catalysis

Relay catalysis requires multiple sites to operate in the same reaction mixture without mutually deactivating one another. To address this problem, Li and co-workers directly polymerized a preformed Au(I)-NHC building block with a chiral secondary-amine-containing monomer [33] (Figure 2B). The resulting imine-linked NHC-Au-SA-COF placed the oxidation catalyst and organocatalyst at distinct framework positions but connected them through a common pore system. This spatial arrangement was intended to prevent strong amine coordination to Au while permitting diffusion of the aldehyde intermediate between the two sites (Scheme 5E). Its porosity, metal loading, and thermal stability are described in Section 2.1.

The two catalytic steps were initially evaluated separately. Aerobic oxidation of an aryl methanol at the Au-NHC site gave the aldehyde quantitatively with 15 mol% Au under air in toluene at 25 °C after 12 h. The secondary amine then catalyzed the asymmetric aldol reaction of the isolated aldehyde in the presence of acetic acid, affording the product in 90% yield and 96% enantiomeric excess at 25 °C. Combining the steps in one vessel eliminated isolation of the aldehyde and established the intended oxidation-aldol relay sequence (Scheme 5E).

Across thirteen aryl methanols, the one-pot sequence furnished products in 69–90% yield and 91–95% enantiomeric excess [33]. After five runs, the recovered powder still provided 86% yield and 94% enantiomeric excess; Au content remained essentially unchanged, and no valence change was detected. These observations are consistent with stable separation of the metal and organocatalytic sites, although direct measurement of the distance between them or of intermediate transport through the pore was not reported.

To improve handling, up to 50 wt% of the COF was dispersed in a chitosan aerogel and freeze-dried as a cup-shaped reactor [33]. On an 8 mmol scale, 1.07 g of alcohol afforded 1.24 g of the aldol product in 82% yield and 95% enantiomeric excess. The shaped catalyst was used five times and still gave 79% yield and 94% enantiomeric excess in the fifth run. This experiment does not establish continuous processing or long-term mechanical stability, but it moves beyond powder recovery and provides the clearest gram-scale demonstration

among the reviewed M-NHC-COFs. A molecular (*S*)-TAPB-MP control gave a comparable aldol outcome (90% yield and 95% ee, versus 90% yield and 96% ee for the COF), so the available data do not demonstrate a substantial framework-induced enhancement in enantioselectivity. The clearest framework-level advantages are co-immobilization of both catalytic functions, catalyst recovery, and macroscopic shaping.

3.6. Photocatalysis

In photocatalytic M-NHC-COF systems, the framework is not merely a support: its donor-acceptor electronic structure generates and separates charge carriers, while the NHC-linked metal site directs interfacial electron transfer and substrate activation. The Cu single-atom CO_2 reduction catalyst and the Au nanocluster H_2O_2 production catalyst represent distinct site nuclearities and should be compared mechanistically rather than ranked by their non-equivalent mass-based rates [51,94,95].

3.6.1. Photocatalytic CO_2 Reduction to Carbon Monoxide

For photochemical CO_2 reduction, the M-NHC unit was incorporated as an electronic junction rather than solely as a catalytic anchor [35]. Mesoporous donor-acceptor pyridine-COF nanosheets were functionalized with imidazolium groups, metalated to NHC-bound Cu(II), and subsequently reduced to Cu(I)-im-pCOF containing 7.8 wt% Cu. Microscopy and X-ray absorption analysis supported atomically dispersed Cu(I) sites. The proposed position of the NHC-linked Cu site within the donor-acceptor architecture is illustrated in Figure 6A. The stepwise PXRD and BET changes produced by functionalization and metalation are compared in Section 2.2 and Table 1.

Under visible light irradiation ($\lambda > 420$ nm) in pure water, without an external photosensitizer or sacrificial electron donor, Cu(I)-im-pCOF converted CO_2 to CO at 184.8 μmol g^{-1} h^{-1} with approximately 100% selectivity, a rate about 22 times that of bulk pCOF [35]. The apparent quantum yield was 1.7% at 420 nm. When the feed was diluted to 10% CO_2 in nitrogen, the catalyst retained 87.5% of its intrinsic activity and an apparent quantum yield of 1.0%, indicating that the mesoporous architecture and Cu site remained effective under a more challenging concentration gradient [35].

The comparison between Cu(I) and Cu(II) states was central. Femtosecond transient absorption spectroscopy gave an electron-transfer rate of 3×10^9 s^{-1} from the electron-rich COF region toward Cu(I) through the NHC linkage. Under reaction conditions, microsecond measurements indicated electron-transfer efficiencies of 60.4% under pure CO_2 and 31.1% under dilute CO_2. In situ infrared spectroscopy detected carboxyl and carbonyl intermediates, while calculations found that Cu(I) lowered the free-energy requirement for the formation of the key carboxyl intermediate. After four cycles, activity declined only slightly and the single-atom coordination environment remained intact. The study demonstrates that ligand placement relative to donor and acceptor units can control the direction and timescale of photogenerated charge flow.

3.6.2. Photocatalytic Hydrogen Peroxide Production

Increasing the metal nuclearity generated a distinct photoactive interface [40]. An imine COF bearing NHC-Au(I) groups was reduced in situ to form Au nanoclusters with an average diameter of 1.66 ± 0.09 nm and a Au loading of 22.67 wt% (Figure 8B). The NHC-containing pores controlled precursor placement and restricted cluster growth, while the cluster-framework contact altered optical absorption and interfacial charge separation. Since reduction converts the original Au(I)-NHC complex into metallic clusters, this system should be classified as an NHC-directed photocatalyst rather than a framework containing

an intact molecular Au-NHC active site. The accompanying PXRD, BET, and pore-size changes are discussed in Section 2.2 and Table 1.

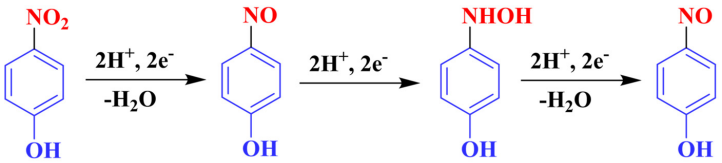
Under visible-light irradiation in air, AuNCs@NHC–COF produced H_2O_2 at 16,565.55 μmol g^{-1} h^{-1} in pH 3 water containing 10 vol% benzyl alcohol [40]. Normalization to the Au content gave a mass activity of 73,072 μmol g Au^{-1} h^{-1}. Benzyl alcohol served as the sacrificial hole scavenger; it was oxidized to benzaldehyde while contributing protons required for oxygen reduction. Methanol, ethanol, and isopropanol also enhanced H_2O_2 production, but none matched the benzyl alcohol–water system. The study reported that a catalyst concentration of 0.25 mg mL^{-1} retained 97% of the maximum production rate; an apparent quantum yield was not reported.

Scavenger experiments, electron paramagnetic resonance, in situ infrared spectroscopy, and electrochemistry supported a two-electron oxygen-reduction pathway. Photogenerated electrons reduce O_2 to superoxide, protonation yields a hydroperoxyl intermediate, and a second electron-proton step forms H_2O_2. The measured electron number was 2.32, consistent with dominant two-electron reduction. Calculations found that Au-O_2 orbital coupling made hydroperoxyl formation favorable, whereas release of H_2O_2 was endergonic. After four cycles, the catalyst retained approximately 85% of its initial rate. The COF and cluster dispersion were largely preserved, but XPS showed partial conversion of Au(0) to Au(I), indicating surface reconstruction or passivation. The high Au loading and dependence on a sacrificial alcohol are therefore the main limitations of an otherwise high rate system.

3.7. Related NHC-Directed Au Nanoparticle Catalysis

One boundary example is informative because it isolates the influence of preparation sequence on metal-particle formation. Gamraoui and co-workers compared the co-assembly of an NHC-Au(I) precursor with the COF monomers against infiltration of the same precursor into an already formed framework [22] (Figure 8A). Reduction in the co-assembled material generated Au particles predominantly in the 1–5 nm range, whereas postsynthetic infiltration led to a broad 1–100 nm distribution and greater agglomeration. Thus, the precursor-incorporation sequence controlled particle nucleation and size; the associated loss of accessible surface area is discussed in Section 2.5.

For p-nitrophenol reduction with sodium borohydride in water, the smaller-particle NHC@AuNP-1@COF showed a reported reaction rate of 3.6×10^{-5} mol min^{-1}, compared with 2.3×10^{-5} mol min^{-1} for the larger-particle material [22]. Although the original article referred to these values as rate constants, the reported units correspond to reaction rates rather than first-order rate constants. Complete conversion occurred in 5 min at room temperature. After five cycles, conversion remained 96%, although the approximately 4% decline was attributed to rearrangement or partial blockage of active sites. The study links the precursor-incorporation sequence to particle size and catalytic response but does not establish an intact molecular Au–NHC active site under turnover conditions (Scheme 6).



Scheme 6. Relationship between COF-confined Au particle size and p-nitrophenol reduction rate.

This material is relevant to M-NHC-COF design because the NHC-Au(I) precursor and COF confinement control particle nucleation and size. It is treated as a boundary case, however, because reduction generates metallic Au particles and the operating catalyst is not an intact molecular Au-NHC complex.

4. Cross-Cutting Structure–Activity Relationships and Mechanistic Evidence

The catalytic scope of NHC-containing COFs extends from metal-free organocatalysis to transformations requiring molecular metal-NHC sites, isolated metal atoms, or NHC-directed metal clusters [52,53]. Metal-free systems are particularly effective in reactions driven by nucleophilic or ionic activation, including CO_2 hydrosilylation, transesterification, epoxide cycloaddition, and Knoevenagel condensation [18,24,25,27]. Incorporation of Au, Cu, Ir, Pd, Rh, or Ru expands this reactivity to redox processes, cross-coupling, bond insertion, C-H activation, and photocatalysis [20,22,31–40]. The reported numerical performances should not, however, be interpreted as a direct activity ranking because the studies differ substantially in substrate identity, catalyst loading, metal normalization, solvent, temperature, pressure, irradiation conditions, and reaction time. Table 3 therefore compares the demonstrated catalytic functions and representative performance metrics while retaining the experimental context required for their interpretation.

Table 3. Catalytic performance of metal-free NHC-containing COFs, molecular M-NHC-COFs, and NHC-directed nanostructures under nonequivalent conditions.

Ref	Active-Site Class	Catalyst and Construction	Transformation	Representative Performance	Reuse and Heterogeneity Evidence
[31]	Molecular/heterogeneous Pd-NHC assignment	Pd@COF-NHC; COF formation then Pd anchoring	Suzuki–Miyaura and aryl bismuth coupling	99% yield; water, room temperature, 1 h, 0.5 mol% Pd	At least 8 cycles; Pd <1 ppm in filtrate
[32]	Molecular Au(I)-NHC	NHC-AuX-COF; direct polymerization and anion exchange	Alkyne carboxylation and hydration	96% carboxylation; 99% hydration	94% yield after 5 cycles; ca. 1% Au loss
[33]	Au(I)-NHC plus chiral aminocatalyst	Chiral NHC-Au-SA-COF; direct copolymerization	Oxidation aldol asymmetric relay	69–90% yields; 91–95% ee; 1.24 g product at 95% ee	5 cycles as powder and shaped aerogel
[34]	Cu(I)-NHC plus NHC-CO_2	COF@NHC-CuCl/CO_2, dual-site PSM	Propargylic-alcohol cyclization and alkyne carboxylation	STY 71.9 h^{-1} at 40 °C; calculated insertion barrier 35.9 → 17.4 kcal mol^{-1}	5 cycles with yields >92%; no Cu in filtrate
[22]	NHC-stabilized Au nanoparticles	NHC@AuNP@COF; precursor incorporated before or after COF formation	p-Nitrophenol reduction	Complete conversion in 5 min; smaller particles reacted faster	96% conversion in cycle 5; negligible Au loss
[20]	Molecular Ir-NHC; Au/Pd analogues	NHC-CO_2 transfer; base-free metalation	CO_2 hydrogenation to formate	Ir: TOF 17,244 h^{-1}; TON 27,015	5 cycles; filtration stopped reaction; isolated Ir retained
[35]	Single Cu(I)-NHC sites	Cu(I)-im-pCOF; postsynthetic anchoring	Photocatalytic CO_2 to CO conversion	184.8 μmol g^{-1} h^{-1}; ca. 100% CO selectivity; AQY 1.7% at 420 nm	4 cycles with negligible decline; Cu(I) coordination retained
[36]	Cu(I)-NHC	Cu(I)-NHC-COF; ionic-liquid grafting and metalation	CO_2 to cyclic carbonates and β-oxopropylcarbamates	>99% conversion/yield at 1 atm; 99% conversion from simulated flue gas in 18 h	10 cycles; 0.08 ppm Cu in filtrate

Table 3. *Cont.*

Ref	Active-Site Class	Catalyst and Construction	Transformation	Representative Performance	Reuse and Heterogeneity Evidence
[37]	Proposed Ru-NHC site; operating coordination sphere and nuclearity not definitively established	Ru-NHC-COF; NHC-CO_2 transfer and metalation	N-H insertion cascade to benzoindoles	78% model yield; 78% on 2 mmol scale	5 cycles; leaching and post-cycle structure not reported
[38,39]	Proposed Pd-NHC sites; molecular Pd-NHC assignment reported, but Pd(0)/cluster contributions not excluded	Pd-NHC-COF; masked-carbene metalation	Suzuki–Miyaura and Mizoroki–Heck coupling	Suzuki: 92% (3 mg catalyst, K_2CO_3, DMF, 120 °C, 24 h); 85% on 3 mmol scale	5 cycles; leaching not reported
[39]	Proposed Rh-NHC and Pd-NHC sites; Rh environment supported, whereas Pd nuclearity remains unresolved	Postsynthetic metalation of NHC-bearing COF	C-H amidation and cross-coupling	Rh amidation: 82% ($AgNTf_2$, DCE, 100 °C, 24 h); Pd coupling: i-PrOH, KOtBu, 60 °C, 12 h	5 Rh cycles; Pd <5 ppm; Pd(0) domains not excluded
[40]	NHC-directed Au nanoclusters	AuNCs@NHC-COF; in situ reduction in bound Au(I)	Photocatalytic H_2O_2 production	16,565.55 μmol g^{-1} h^{-1} in pH 3 water/10 vol% benzyl alcohol under visible light and air; AQY not reported	Ca. 85% activity after 4 cycles; partial Au oxidation
[18]	Metal-free NHC generated from NHC-CO_2	COF-NHC- CO_2; thermal unmasking	CO_2 hydrosilylation and N-formylation	>90% methanol; TOF 66.7 and 76.8 h^{-1} at 0.1 MPa CO_2 and 60 °C	At least 3 cycles without loss; filtration stopped reaction
[24]	Metal-free base-generated NHC	NHC-Py-COF generated with Na_2CO_3	Glycerol transesterification	DMC: 99% conversion, 96% yield; 70 C, 8 h, 5 mol% catalyst	5 cycles; final conversion/yield 95%/93%
[25]	Ionic benzimidazolium bromide	BMIM4F-Py-COF; quaternized precursor	CO_2-epoxide cycloaddition	Up to 100% yield; TON 608; 4.0 MPa, 110 C, 12 h	5 cycles; catalyst removal stopped conversion
[27]	Ionic/basic COF (Knoevenagel); KOtBu-generated NHC proposed for lactone synthesis	Por-NHC-COF; KOtBu activation for lactone synthesis	Knoevenagel condensation and γ-butyrolactone synthesis	>99% in 1 h at room temperature; lactone 90% in 12 h	6 Knoevenagel cycles; filtration stopped conversion

The performance comparison highlights complementary rather than competing catalytic roles. Metal-free NHC and benzimidazolium frameworks exploit nucleophilicity, basicity, or ion-pair activation, whereas metal-containing systems add redox chemistry, bond insertion, cross-coupling, and photochemical charge transfer. Catalytic activity has been reported for materials with widely different surface areas, suggesting that accessible site density, pore connectivity, and local substrate enrichment can be more informative than BET area alone. At the same time, yields, TONs, TOFs, space-time yields, and photocatalytic production rates cannot be compared quantitatively unless the reaction and normalization conventions are equivalent.

Catalyst durability likewise cannot be established from recycling data alone. The strongest studies combine repeated-use experiments with hot filtration or catalyst removal

tests, quantitative metal leaching measurements where applicable, and post-reaction characterization of both the framework and the proposed active site. This combined evidence is particularly strong for the Ir- and Cu-NHC systems [20,36] and for the metal-free frameworks [18,25,27]. By contrast, recycling without leaching analysis or post-reaction spectroscopy confirms recoverability but does not establish retention of a molecular M-NHC site or an intact free-carbene state [24,37,38]. The Au nanocluster system further shows that a catalyst can remain heterogeneous while its metal surface undergoes partial oxidation [40]. Table 4 therefore distinguishes operational reuse from stronger evidence for heterogeneity and active-site preservation.

Table 4. Recyclability, catalyst loss, and evidence for heterogeneous catalysis.

Ref	Catalyst	Reuse Result	Leaching, Filtration, or Catalyst-Loss Evidence	Post-Reaction Structural Evidence	Reliability Assessment
[31]	Pd@COF-NHC	At least 8 cycles without significant loss	Hot filtration: 46.9% at removal, 47.5% after 1 h, and 48.6% after 4 h; Pd <1 ppm (<0.05% inventory)	TEM morphology/Pd dispersion and XPS retained after eight cycles; post-cycle PXRD/BET not reported	Strong evidence against a persistent dissolved Pd pool; crystalline Pd domains complicate active-site assignment
[32]	NHC-AuCl-COF	94% yield in cycle 5	Ca. 1% Au loss	PXRD and morphology retained	Good short-term retention; longer cycling needed
[33]	NHC-Au-SA-COF	Powder: 86% yield/94% ee after 5 runs; shaped form: 79%/94% ee in run 5	Au content essentially unchanged	Metal valence retained	Strong because activity, ee, shaping, and Au content were followed
[34]	COF@NHC-CuCl/CO_2	Yields >92% over 5 cycles	No Cu detected in filtrate	(010) retained; several higher-order reflections disappeared	Catalytic stability convincing; complete crystallinity retention not demonstrated
[22]	NHC@AuNP@COF	96% conversion in cycle 5	Negligible Au loss	Particle size/distribution remained the key activity descriptor	Supports particle retention, but the operating site is a nanoparticle surface rather than a molecular Au-NHC
[20]	Ir-NHC-COF	Activity unchanged after 5 uses	Filtration after 4 or 8 h stopped further formate formation	BET 507 -> 483 m^2 g^{-1}; microscopy, XPS, and XAS retained isolated Ir	Strong combined heterogeneity and local-structure evidence
[35]	Cu(I)-im-pCOF	4 cycles with slight decline	Not reported	Single-atom coordination retained	Good site-stability evidence; no quantitative leaching value
[36]	Cu(I)-NHC-COF	10 cycles with small decline	0.08 ppm Cu in filtrate	FT-IR, PXRD, SEM, and XPS matched pristine catalyst	Among the strongest durability datasets
[37]	Ru-NHC-COF	5 cycles after filtration and washing	Not reported	Not reported	Reuse shown; leaching and structural retention insufficiently tested; operating Ru site not verified operando

Table 4. *Cont.*

Ref	Catalyst	Reuse Result	Leaching, Filtration, or Catalyst-Loss Evidence	Post-Reaction Structural Evidence	Reliability Assessment
[38]	Pd-NHC-COF	5 cycles	Not reported	Not reported	Recycling alone does not establish true heterogeneity or retained Pd-NHC structure; molecular Pd-NHC site not verified operando
[39]	Rh- and Pd-NHC-COFs	5 Rh cycles; Pd reused	Pd <5 ppm; bulk Pd 20.4 -> 19.8 wt%	Granular Pd-rich regions remain possible	Low dissolved Pd shown; molecular, cluster, and Pd(0) contributions unresolved; Pd nuclearity remains unresolved
[40]	AuNCs@NHC-COF	Ca. 85% initial rate after 4 cycles	Not reported	PXRD mostly retained; clusters dispersed; partial Au(0) -> Au(I)	Cluster retention supported; surface reconstruction accompanies deactivation
[18]	COF-NHC-CO_2	At least 3 cycles without activity or selectivity loss	Filtration after 3 h gave negligible further yield	PXRD and porosity retained; ^{13}C NMR showed regenerated NHC-CO_2	Strong heterogeneity and active-site regeneration evidence for a metal-free catalyst
[24]	NHC-Py-COF	Recycle run 1: 99%/95%; run 5: 95%/93% (fresh catalyst: 99%/96%).	Not reported	Not reported	Useful reuse data; heterogeneity and post-cycle structure need stronger verification
[25]	BMIM4F-Py-COF	5 cycles without significant activity/selectivity loss	Mid-reaction catalyst removal stopped conversion	PXRD and FT-IR unchanged after 5 runs	Strong short-term heterogeneity and framework-retention evidence
[27]	Por-NHC-COF	6 Knoevenagel cycles without significant activity loss	Removal after 30 min stopped further yield increase	PXRD retained after 6 runs; high activity after acid/base soaking	Strong short-term heterogeneity and chemical-stability evidence

Mechanistic confidence also varies substantially among catalyst classes. The most persuasive assignments combine control reactions with direct observation of intermediates or charge-transfer dynamics and computational evaluation of the proposed elementary steps. Cu(I)-im-pCOF provides particularly strong evidence through femtosecond and microsecond transient-absorption spectroscopy, in situ infrared detection of reaction intermediates, oxidation-state controls, and DFT calculations [35]. The metal-free COF-NHC-CO_2 system likewise combines isotopic labeling, in situ spectroscopy, catalyst removal experiments, and calculated activation barriers [18]. Complementary experimental and computational results also support the cooperative Cu catalyst, isolated Ir-NHC sites, Ru insertion catalyst, and Au nanocluster photocatalyst [20,34,37,40]. In other cases, catalytic cycles rely mainly on product distributions, controls, or precedent from homogeneous chemistry. Table 5 grades the available evidence without treating a computationally plausible or author-proposed pathway as experimentally proven.

Table 5. Strength of mechanistic evidence in metal-free and metal-containing NHC–COF catalyst classes.

Ref	Mechanistic Claim	Direct Experimental Support	Computational Support	Evidence Grade and Principal Uncertainty
[32]	Au(I)-NHC activates terminal alkyne; counterion controls aqueous hydration	Product scope, anion exchange, contact-angle and control comparisons	Not reported	Moderate; counterion alters both wettability and Au electrophilicity
[34]	NHC-CuCl activates alkyne while NHC-CO_2 supplies activated CO_2	Single-site controls and spectroscopic assignment of both functions	Insertion barriers 35.9 → 17.4 and 50.8 → 30.2 kcal mol^{-1}	Strong for cooperative benefit; exact turnover-site geometry remains modeled
[20]	Electron-rich isolated Ir-NHC promotes H_2 activation and CO_2 insertion	Homogeneous and physical-mixture controls; XAS identifies isolated Ir; filtration	Calculated Ir-H/CO_2 pathway and favorable electronic structure	Strong; operando confirmation of intermediates absent
[35]	NHC bridge directs photogenerated electrons to Cu(I) for CO_2 to CO conversion	Femtosecond/microsecond transient absorption; in situ IR; oxidation-state controls	Free-energy profile for carboxyl intermediate	Strong according to the evidence rubric used in this review
[36]	Cu(I) activates propargylic alcohol; N-rich framework enriches CO_2	Catalyst and CuCl controls; cyclic-carbonate intermediate identified	Not reported	Moderate; cooperative framework role inferred, not spatially resolved
[37]	Cationic Ru-carbene undergoes N-H insertion followed by cyclization	HRMS detection of N-H insertion intermediate and control experiments	Binding and migratory-insertion energetics	Moderate to strong; later rearrangement/dehydration steps remain proposed
[39]	Rh(III) undergoes directed C-H activation, nitrene insertion, and protonation	Substrate selectivity and catalyst controls	Calculated C–H activation barrier 19.8 kcal mol^{-1}	Moderate; no operando intermediate detection
[40]	Au clusters accelerate two-electron O_2 reduction to H_2O_2	EPR, scavenger tests, in situ IR, charge-transfer measurements, electron number 2.32	Au-O_2 and hydroperoxyl energetics	Strong for dominant two-electron pathway; alcohol oxidation and Au reconstruction complicate kinetics
[18]	Thermally exposed NHC attacks silane before CO_2 insertion	$^{13}CO_2$ labeling; in situ FT-IR identifies formoxysilane RDS; precursor and filtration controls	Silane-first barrier 22.2 vs. CO_2-first barrier 32.6 kcal mol^{-1}; DOS/ESP analysis	Strong; best-supported metal-free mechanism in the set
[24]	Free NHC attacks dialkyl carbonate; methoxide deprotonates glycerol; acyl transfer closes the cycle	No product with BMIMBr, IM4F-Py-COF, 4F-Py-COF, or no catalyst	Not reported	Moderate for NHC requirement; intermediates and elementary steps remain proposed
[25]	Bromide opens epoxide; CO_2 insertion and ring closure yield cyclic carbonate	Catalyst-removal test and substrate scope	Not reported	Low to moderate; pathway follows ionic-liquid precedent without direct intermediate detection

Table 5. *Cont.*

Ref	Mechanistic Claim	Direct Experimental Support	Computational Support	Evidence Grade and Principal Uncertainty
[27]	Framework basic/ionic sites promote Knoevenagel condensation; base-generated NHC forms a homoenolate for lactone synthesis	Monomer/blank controls; no product without COF in lactone reaction; filtration test; strong-base dependence	Not reported	Moderate for catalyst-state assignment; detailed intermediates are proposed from literature precedent

Taken together, the comparisons in Tables 3–5 reveal several recurring relationships between active site structure, framework environment, and catalytic behavior. Strong NHC coordination was generally associated with limited metal loss in the systems for which quantitative leaching or post-reaction metal analysis was reported [20,32–34,36,39]. Comparable leaching evidence was not reported for Ru-NHC-COF. This association does not prove that the original molecular M-NHC site remains unchanged throughout catalysis, particularly when reaction conditions can alter metal oxidation state or coordination. A corresponding distinction is required for metal-free systems, in which imidazolium, free NHC, and CO_2-masked NHC sites represent chemically different catalytic states rather than interchangeable descriptions of the same active center [18,24,25,27].

Porosity influences catalytic performance in ways that are not adequately described by BET surface area alone. Pd@COF-NHC remained highly active despite its relatively low accessible surface area [31], whereas other systems benefited from mesoporous transport, CO_2 enrichment, exposure of isolated metal sites, or confinement of metal clusters [34–36,40]. Accessible active site density, pore connectivity, substrate diffusion, and the spatial distribution of catalytic sites are therefore more useful descriptors than total surface area considered in isolation. This comparison also explains why a decrease in BET area after postsynthetic modification does not necessarily reduce activity when functionalization creates a more effective local reaction environment.

The pore microenvironment can further regulate activity and selectivity. Counterion exchange in NHC-Au COFs altered wettability and enabled efficient Au-catalyzed hydration in water [32], while the chiral framework preserved high enantioselectivity while enabling co-immobilization and shaping, although a molecular control showed a comparable *ee* [33]. In dual-site Cu systems, immobilized NHC-CO_2 adducts facilitated local CO_2 delivery and lowered the calculated barrier for carboxylation [34]. Positioning NHC-bound Cu(I) sites near the electron-accepting region of a donor-acceptor COF promoted directional transfer of photogenerated electrons [35]. Metal-free examples extend the same principle: reversible CO_2 masking protects a reactive carbene until thermal activation [18], whereas benzimidazolium/bromide ion pairs promote cooperative epoxide activation and nucleophilic ring opening [25]. Thus, the framework can control polarity, reactant concentration, stereochemical environment, ionic organization, and charge-transfer distance rather than acting solely as an inert support.

Metal nuclearity must be considered both a design parameter and a possible variable under operating conditions. Strong chelation and spatial separation can favor molecular or single-atom sites, whereas reduction in framework-bound precursors may intentionally generate Au nanoparticles or nanoclusters [22,40]. Similar transformations may occur unintentionally during Pd-catalyzed cross-coupling, where molecular Pd(II)-NHC sites, subnanometer clusters, and Pd(0) domains may coexist or interconvert [31,38,39]. A catalyst may therefore remain recoverable and heterogeneous even when the chemical identity of its operating site changes. Hot filtration and low metal concentrations in the filtrate can

exclude a persistent dissolved-metal pool as the dominant catalyst, but they cannot by themselves distinguish molecular sites, isolated atoms, clusters, and nanoparticle surfaces. Establishing the operating structure requires these tests to be combined with post-reaction and, preferably, operando characterization.

5. Remaining Challenges and Future Perspectives

The literature establishes the feasibility of both metal-free NHC-COFs and metal-containing M-NHC-COFs, but comparison and scale-up remain limited by inconsistent performance reporting. Studies variously report isolated yield, conversion, TON, TOF, space-time yield, apparent quantum yield, or production rate per mass of total catalyst. Metal-containing systems should report total and accessible metal site concentrations together with metal-normalized and catalyst mass-normalized rates. Metal-free systems require analogous quantification of accessible imidazolium, free-carbene, or NHC-CO_2 sites and should distinguish the amount of added base from the concentration of framework-generated carbene. For photocatalysis, photon flux, illuminated area, optical path length, and wavelength-dependent quantum yields are essential for meaningful comparisons [96].

A second challenge is identifying the operating active site under reaction conditions. For metal-containing materials, ex situ XPS, microscopy, PXRD, and elemental mapping may miss transient reduction, ligand exchange, coordination changes, or subnanometer clustering. Operando X-ray absorption and vibrational spectroscopy should therefore be combined with kinetic measurements and time-resolved leaching analysis [65,97]. Metal-free catalysts present a different but equally important assignment problem: imidazolium salts, free NHCs, NHC-CO_2 adducts, residual homogeneous base, and framework basic sites can produce overlapping reactivity. Carbene trapping, isotopic labeling, quantitative solid-state NMR, acid–base titration, and catalyst-removal controls are needed to establish whether a framework-bound NHC is actually generated and remains responsible for turnover.

Sustainability claims must also account for the complete reaction and catalyst-preparation sequence [98]. Several high-performing metal-containing systems require cesium carbonate, DBU, DMF, dichloroethane, silver activators, sacrificial alcohols, or pressurized CO_2/H_2, while some nominally metal-free catalysts depend on strong bases such as KOtBu or on energy-intensive thermal unmasking. Avoiding noble metals is an advantage only if it is not offset by hazardous bases, difficult monomer synthesis, low site utilization, or solvent-intensive purification. Future work should prioritize aqueous or bio-derived solvents, lower base and cocatalyst loadings, silver-free activation, direct use of dilute CO_2, and complete mass and energy balances.

Framework stability must be evaluated beyond retention of a small number of diffraction peaks [65]. Imine-linked COFs dominate the current literature because they are synthetically accessible, but water, acid, base, light, and redox cycling can change linkage chemistry, long-range order, pore accessibility, and active-site identity. Metal-containing catalysts additionally require monitoring of oxidation state, coordination number, aggregation, and leaching. Metal-free systems should be examined for carbene protonation, dimerization, loss of counterions, and reversibility of masking or activation. Mass recovery, pore-volume retention, linkage-specific spectroscopy, active-site quantification, and testing over tens rather than three to six cycles would provide a more realistic durability assessment.

Catalyst economy should be evaluated differently for the two material classes. Cu-based systems show that earth-abundant metals can support thermal CO_2 fixation and photocatalytic reduction [34–36], whereas the high Au loading in AuNCs@NHC-COF increases material cost despite its high H_2O_2 production rate [40]. Fe-, Co-, Ni-, and Mn–NHC COFs are therefore important targets, provided that their oxidation states and coordination environments can be stabilized. Metal-free NHC-COFs avoid metal cost and

contamination, but their practical advantage must be demonstrated against inexpensive homogeneous organobases and ionic liquids on the basis of site productivity, recovery, preparation complexity, and lifetime.

Scalable synthesis and catalyst shaping remain underdeveloped across both families. Most materials are prepared over several days in sealed tubes and require repeated solvent washing and activation. Continuous or flow-assisted COF synthesis, solvent recovery, lower-temperature crystallization [99,100], and batch-to-batch criteria for crystallinity, porosity, and active-site loading are needed. Pellets, monoliths, membranes, aerogels, or coated supports should preserve pore accessibility and site distribution while providing adequate mechanical strength. The chitosan aerogel reactor demonstrates the feasibility of catalyst shaping [33], but pressure drop, residence-time distribution, long-duration operation, and mechanical degradation remain to be evaluated.

The catalytic scope should expand beyond the present emphasis on CO_2 conversion and cross-coupling. Metal-free frameworks could be developed for umpolung chemistry, acyl transfer, polymerization, and cooperative acid–base catalysis, whereas metal-containing systems offer opportunities in asymmetric hydrogenation, allylic substitution, cyclopropanation, selective oxidation, and stereoselective C-H functionalization [101]. Chiral NHCs, chiral pore environments, and controlled spacing between organocatalytic and metal sites may enable reactions that require sequential or mutually incompatible catalytic functions. Industrially relevant studies should use less activated substrates, concentrated mixtures, impure or dilute feeds, and product-isolation protocols that quantify productivity, catalyst carryover, and, where applicable, metal contamination.

Future catalyst development should be guided by testable structure-function hypotheses rather than comparisons among unrelated frameworks. Systematic variation in NHC electronics, precursor state, counterion, pore size, active-site density, metal identity, nuclearity, and intersite spacing while holding other variables constant would establish more reliable design rules. Combined operando spectroscopy, kinetics, isotopic experiments, and computation can then determine whether the intended free NHC, ionic, molecular M-NHC, single-atom, or cluster state remains responsible for turnover.

6. Conclusions

NHC-containing COFs now encompass three related but chemically distinct catalyst classes: metal-free materials in which a framework-bound NHC precursor, free carbene, or ionic pair participates directly in organocatalysis; molecular M-NHC materials in which the NHC coordinates and electronically regulates a metal center; and NHC-directed metal nanoparticles or nanoclusters in which the carbene-containing framework controls precursor binding, nucleation, or confinement without necessarily remaining as an intact molecular M-NHC site. Across these classes, direct polymerization provides deliberate placement of preformed functional units, whereas postsynthetic modification offers broader modularity and permits precursor installation, carbene generation, or metalation after framework formation. CO_2-masked carbenes are particularly important because they enable controlled NHC release and base-free transfer to metal precursors.

Metal-free NHC-COFs demonstrate that a crystalline porous framework can stabilize and spatially separate reactive carbene or ionic catalytic sites. Thermal unmasking, base-induced carbene generation, and benzimidazolium/bromide cooperation have enabled CO_2 hydrosilylation, N-formylation, transesterification, cyclic-carbonate formation, Knoevenagel condensation, and γ-butyrolactone synthesis. Their principal advantages are avoidance of metal contamination and access to organocatalytic reaction modes, but the identity and concentration of the active carbene must be distinguished carefully from precursor ions, framework basicity, and residual homogeneous base.

Metal-containing M-NHC-COFs extend this platform to transformations requiring redox activity, bond insertion, cross-coupling, or photogenerated charge transfer. Molecular Au, Cu, Ir, Pd, Rh, and Ru sites support CO_2 conversion, C-C coupling, C-H and N-H functionalization, and asymmetric relay catalysis, while Cu single atoms and Au nanoclusters create photoactive interfaces for CO_2 reduction and H_2O_2 production. In molecular systems, the NHC can control coordination and electronic structure, whereas the COF can contribute confinement, mass transport, site separation, and a programmable microenvironment; for reduced nanoparticles and nanoclusters, however, the NHC primarily directs precursor localization and particle stabilization rather than defining an intact molecular metal-carbene site. The strongest examples exploit these functions cooperatively rather than using the framework as a passive support.

The collective evidence also defines the limits of current structure-activity claims. Retention of PXRD reflections does not establish preservation of pore accessibility, and recycling alone does not prove that the proposed active site remains intact. For molecular metal sites, hot filtration and low leaching exclude only a persistent dissolved-metal reservoir and cannot distinguish molecular complexes from clusters or nanoparticles. For metal-free materials, catalyst removal and reuse must be complemented by direct evidence for carbene generation, regeneration, and resistance to protonation or dimerization. Reliable assignment therefore requires convergent diffraction, gas sorption, spectroscopic, microscopic, kinetic, and post-reaction evidence.

Progress toward practical NHC-COF catalysis will depend on standardized activity normalization, robust linkages, scalable synthesis, shaped reactors, long-term testing, and operando identification of the active state. Earth-abundant M-NHC sites and genuinely metal-free catalysts offer complementary routes to lower material cost and contamination, but both must be evaluated against simpler homogeneous alternatives. Systematic control of NHC electronics, pore environment, site density, and cooperative-site spacing should ultimately transform NHC-containing COFs from isolated proof-of-concept catalysts into a broadly applicable platform for recyclable molecular and organocatalytic reactivity.

Funding: This research received no external funding.

Data Availability Statement: No new data were created or analyzed in this study. Data sharing is not applicable to this article.

Conflicts of Interest: The authors declare no conflict of interest.

References

1. Geng, K.; He, T.; Liu, R.; Dalapati, S.; Tan, K.T.; Li, Z.; Tao, S.; Gong, Y.; Jiang, Q.; Jiang, D. Covalent Organic Frameworks: Design, Synthesis, and Functions. *Chem. Rev.* **2020**, *120*, 8814–8933. [CrossRef] [PubMed]
2. Yusran, Y.; Miao, B.; Qiu, S.; Fang, Q. Functional Covalent Organic Frameworks: Design Principles to Potential Applications. *Acc. Mater. Res.* **2024**, *5*, 1263–1278. [CrossRef]
3. Côté, A.P.; Benin, A.I.; Ockwig, N.W.; O'Keeffe, M.; Matzger, A.J.; Yaghi, O.M. Porous, Crystalline, Covalent Organic Frameworks. *Science* **2005**, *310*, 1166–1170. [CrossRef] [PubMed]
4. Khojastehnezhad, A.; Bisio, A.; Rafie, S.F.; Jafari, M.; Peng, Z.; Shehab, M.K.; Abu-Zahra, N.; Farha, O.K.; Siaj, M. Hierarchical Design of COFs via NHC-Grafting for Selective Gold Recovery from E-Waste: Experimental and MD Analyses. *J. Am. Chem. Soc.* **2025**, *147*, 38516–38533. [CrossRef] [PubMed]
5. Nejabat, M.; Samie, A.; Khojastehnezhad, A.; Hadizadeh, F.; Ramezani, M.; Alibolandi, M.; Abnous, K.; Taghdisi, S.M.; Siaj, M. Stimuli-Responsive Covalent Organic Frameworks for Cancer Therapy. *ACS Appl. Mater. Interfaces* **2024**, *16*, 51837–51859. [CrossRef] [PubMed]
6. Rhouati, A.; Al Mogren, M.; Teniou, A.; Elwary, S.; Khojastehnezhad, A.; Siaj, M.; Zourob, M. Electrochemical selection of a CFTR-specific aptamer and design of a COF-based aptasensor for the diagnosis of cystic fibrosis. *Nanoscale* **2025**, *17*, 25336–25347. [CrossRef] [PubMed]

7. Khojastehnezhad, A.; Rhili, K.; Shehab, M.K.; Gamraoui, H.; Peng, Z.; Samih ElDouhaibi, A.; Touzani, R.; Hammouti, B.; El-Kaderi, H.M.; Siaj, M. Rapid, Mild, and Catalytic Synthesis of 2D and 3D COFs with Promising Supercapacitor Applications. *ACS Appl. Energy Mater.* **2023**, *6*, 12216–12225. [CrossRef]
8. Jafari, M.; Peng, Z.; Samie, A.; Taghavi, F.; Khojastehnezhad, A.; Siaj, M. Catalyst-Driven Improvements in Conventional Methods for Imine-Linked Covalent Organic Frameworks. *Molecules* **2025**, *30*, 2969. [CrossRef] [PubMed]
9. Khojastehnezhad, A.; Moeinpour, F.; Jafari, M.; Shehab, M.K.; Samih ElDouhaibi, A.; El-Kaderi, H.M.; Siaj, M. Postsynthetic modification of core–shell magnetic covalent organic frameworks for the selective removal of mercury. *ACS Appl. Mater. Interfaces* **2023**, *15*, 28476–28490. [CrossRef] [PubMed]
10. Waller, P.J.; Gándara, F.; Yaghi, O.M. Chemistry of Covalent Organic Frameworks. *Acc. Chem. Res.* **2015**, *48*, 3053–3063. [CrossRef] [PubMed]
11. Rose, M.; Palkovits*, R. Catalysis by Covalent Organic Frameworks (COFs). In *Metal Organic Frameworks as Heterogeneous Catalysts*; Llabres i Xamena, F., Gascon, J., Eds.; The Royal Society of Chemistry: London, UK, 2013; pp. 384–405.
12. Yang, J.; Wang, B.; Feng, X. Mass Transport Based on Covalent Organic Frameworks. *Acc. Chem. Res.* **2025**, *58*, 1447–1460. [CrossRef] [PubMed]
13. Sun, Q.; Tang, Y.; Aguila, B.; Wang, S.; Xiao, F.S.; Thallapally, P.K.; Al-Enizi, A.M.; Nafady, A.; Ma, S. Reaction environment modification in covalent organic frameworks for catalytic performance enhancement. *Angew. Chem.* **2019**, *131*, 8762–8767. [CrossRef]
14. Ohmiya, H. N-Heterocyclic Carbene-Based Catalysis Enabling Cross-Coupling Reactions. *ACS Catal.* **2020**, *10*, 6862–6869. [CrossRef]
15. Miyabe, H. Recent Advances in Cooperative N-Heterocyclic Carbene Catalysis. In *Carbene*; IntechOpen: London, UK, 2021.
16. Hopkinson, M.N.; Richter, C.; Schedler, M.; Glorius, F. An overview of N-heterocyclic carbenes. *Nature* **2014**, *510*, 485–496. [CrossRef] [PubMed]
17. Liu, T.T.; Xu, R.; Yi, J.D.; Liang, J.; Wang, X.S.; Shi, P.C.; Huang, Y.B.; Cao, R. Imidazolium-Based Cationic Covalent Triazine Frameworks for Highly Efficient Cycloaddition of Carbon Dioxide. *ChemCatChem* **2018**, *10*, 2036–2040. [CrossRef]
18. He, C.; Si, D.H.; Huang, Y.B.; Cao, R. A CO_2-masked carbene functionalized covalent organic framework for highly efficient carbon dioxide conversion. *Angew. Chem.* **2022**, *134*, e202207478. [CrossRef]
19. Gunasekar, G.H.; Park, K.; Ganesan, V.; Lee, K.; Kim, N.-K.; Jung, K.-D.; Yoon, S. A Covalent Triazine Framework, Functionalized with Ir/N-Heterocyclic Carbene Sites, for the Efficient Hydrogenation of CO_2 to Formate. *Chem. Mater.* **2017**, *29*, 6740–6748. [CrossRef]
20. He, C.; Si, D.-H.; Han, L.; Xu, Z.-N.; Chen, Z.; Cao, R.; Huang, Y.-B. A General Base-free Route toward the Building of Metal N-Heterocyclic Carbenes into Covalent Organic Frameworks for CO_2 Conversion. *ACS Catal.* **2024**, *14*, 3943–3954. [CrossRef]
21. Díez-González, S.; Marion, N.; Nolan, S.P. N-Heterocyclic Carbenes in Late Transition Metal Catalysis. *Chem. Rev.* **2009**, *109*, 3612–3676. [CrossRef] [PubMed]
22. Gamraoui, H.; Khojastehnezhad, A.; Bélanger-Bouliga, M.; Nazemi, A.; Siaj, M. Covalent Organic Framework-Templated N-Heterocyclic Carbene-Functionalized Gold Nanoparticles for the Catalytic Reduction of Nitrophenol. *ACS Appl. Nano Mater.* **2024**, *7*, 22570–22580. [CrossRef]
23. Hu, H.; Yan, Q.; Ge, R.; Gao, Y. Covalent organic frameworks as heterogeneous catalysts. *Chin. J. Catal.* **2018**, *39*, 1167–1179. [CrossRef]
24. Chai, Y.; Li, Y.; Hu, H.; Zeng, C.; Wang, S.; Xu, H.; Gao, Y. N-Heterocyclic Carbene Functionalized Covalent Organic Framework for Transesterification of Glycerol with Dialkyl Carbonates. *Catalysts* **2021**, *11*, 423. [CrossRef]
25. Yan, Q.; Liang, H.; Wang, S.; Hu, H.; Su, X.; Xiao, S.; Xu, H.; Jing, X.; Lu, F.; Gao, Y. Immobilization of ionic liquid on a covalent organic framework for effectively catalyzing cycloaddition of CO_2 to epoxides. *Molecules* **2022**, *27*, 6204. [CrossRef] [PubMed]
26. Qiu, J.; Zhao, Y.; Li, Z.; Wang, H.; Shi, Y.; Wang, J. Imidazolium-salt-functionalized covalent organic frameworks for highly efficient catalysis of CO_2 conversion. *ChemSusChem* **2019**, *12*, 2421–2427. [CrossRef] [PubMed]
27. Zhang, W.; Wang, B.; Feng, S.; Feng, H.; Bai, J.; Wang, J. An N-heterocyclic carbene functional covalent organic framework for Knoevenagel condensation reaction and γ-butyrolactone synthesis at room temperature. *New J. Chem.* **2024**, *48*, 16813–16819. [CrossRef]
28. Zhao, Y.; Zhao, Y.; Qiu, J.; Li, Z.; Wang, H.; Wang, J. Facile Grafting of Imidazolium Salt in Covalent Organic Frameworks with Enhanced Catalytic Activity for CO_2 Fixation and the Knoevenagel Reaction. *ACS Sustain. Chem. Eng.* **2020**, *8*, 18413–18419. [CrossRef]
29. Huang, N.; Wang, P.; Addicoat, M.A.; Heine, T.; Jiang, D. Ionic covalent organic frameworks: Design of a charged interface aligned on 1D channel walls and its unusual electrostatic functions. *Angew. Chem.* **2017**, *129*, 5064–5068. [CrossRef]
30. Chakraborty, D.; Mullangi, D.; Chandran, C.; Vaidhyanathan, R. Nanopores of a Covalent Organic Framework: A Customizable Vessel for Organocatalysis. *ACS Omega* **2022**, *7*, 15275–15295. [CrossRef] [PubMed]

31. Yang, J.; Wu, Y.; Wu, X.; Liu, W.; Wang, Y.; Wang, J. An N-heterocyclic carbene-functionalised covalent organic framework with atomically dispersed palladium for coupling reactions under mild conditions. *Green Chem.* **2019**, *21*, 5267–5273. [CrossRef]
32. Li, Y.; Dong, Y.; Kan, J.-L.; Wu, X.; Dong, Y.-B. Synthesis and Catalytic Properties of Metal–N-Heterocyclic-Carbene-Decorated Covalent Organic Framework. *Org. Lett.* **2020**, *22*, 7363–7368. [CrossRef] [PubMed]
33. Li, Y.; Wang, J.-M.; Kan, J.-L.; Li, F.; Dong, Y.; Dong, Y.-B. Combination of a Metal-N-Heterocyclic-Carbene Catalyst and a Chiral Aminocatalyst within a Covalent Organic Framework: A Powerful Cooperative Approach for Relay Asymmetric Catalysis. *Inorg. Chem.* **2022**, *61*, 2455–2462. [CrossRef] [PubMed]
34. Guo, X.; Zhang, F.; Yang, Z.; Gao, L.; Wei, R.; Xiao, G. Construction of covalent organic framework functionalized with carbene dual active sites for enhancing CO_2 carboxylation conversion. *Chem. Eng. J.* **2023**, *475*, 146453. [CrossRef]
35. Liu, Z.; Yin, H.; Sun, J.; Bai, L.; Li, Z.; Zhao, X.; Yan, X.; Zhao, M.; Jing, L. Engineering single Cu atoms anchored via N-heterocyclic carbene in COF mesopores for modulating electron kinetics of CO_2 photoconversion. *Adv. Energy Mater.* **2024**, *14*, 2401713. [CrossRef]
36. Parihar, V.; Rani, P.; Kumar, S.; Beniwal, P.; Nagaraja, C.M. Cu (I)-Anchored NHC-Functionalized Covalent Organic Framework (COF) for Catalyzing CO_2 Chemical Fixation into High-Value Compounds. *Inorg. Chem.* **2025**, *64*, 24834–24843. [CrossRef] [PubMed]
37. Wang, X.; Fan, F.; Hu, M.; Qiao, C.; Cao, B.; Gong, X.; Szostak, M. Ruthenium/N–Heterocyclic carbene-decorated covalent organic framework for N–H insertion cascade nucleophilic cyclization. *J. Catal.* **2025**, *448*, 116211. [CrossRef]
38. Wang, X.; Li, J.; Wang, L.; Szostak, M. Palladium/N-Heterocyclic Carbene-Decorated Covalent Organic Framework for Suzuki–Miyaura and Mizoroki–Heck Cross-Coupling. *J. Org. Chem.* **2025**, *90*, 6532–6537. [CrossRef] [PubMed]
39. Wang, X.; Gong, X.; Cao, B.; Yan, F.; Zhang, R.; Li, Z.; Yang, S.; Zhou, C.; Szostak, M. Metal/N-Heterocyclic Carbene-Decorated Covalent Organic Framework for C–H Amidation and Cross-Coupling. *ACS Sustain. Chem. Eng.* **2026**, *14*, 7509–7517. [CrossRef]
40. Ma, J.; Cai, Z.; Xiao, Y.; Zhang, X.; Shu, T. Enhancing photocatalytic H_2O_2 production using high-loading Au nanoclusters in N-heterocyclic carbene decorated covalent organic frameworks. *Nano Res.* **2026**, *19*, 94908902. [CrossRef]
41. Rogge, S.M.J.; Bavykina, A.; Hajek, J.; Garcia, H.; Olivos-Suarez, A.I.; Sepúlveda-Escribano, A.; Vimont, A.; Clet, G.; Bazin, P.; Kapteijn, F.; et al. Metal–organic and covalent organic frameworks as single-site catalysts. *Chem. Soc. Rev.* **2017**, *46*, 3134–3184. [CrossRef] [PubMed]
42. Chen, C.; Cao, L.; Liu, Y.; Li, Z.; Li, Z.-H.; Zhou, G.; Zhang, D.; Huang, X.; Wang, Y.; Li, G.; et al. Investigating a Seemingly Simple Imine-Linked Covalent Organic Framework Structure. *J. Am. Chem. Soc.* **2024**, *146*, 35504–35512. [CrossRef] [PubMed]
43. Khojastehnezhad, A.; Samie, A.; Bisio, A.; El-Kaderi, H.M.; Siaj, M. Impact of Postsynthetic Modification on the Covalent Organic Framework (COF) Structures. *ACS Appl. Mater. Interfaces* **2025**, *17*, 11415–11442. [CrossRef] [PubMed]
44. Yusran, Y.; Guan, X.; Li, H.; Fang, Q.; Qiu, S. Postsynthetic functionalization of covalent organic frameworks. *Natl. Sci. Rev.* **2020**, *7*, 170–190. [CrossRef] [PubMed]
45. Crabtree, R.H. Resolving Heterogeneity Problems and Impurity Artifacts in Operationally Homogeneous Transition Metal Catalysts. *Chem. Rev.* **2012**, *112*, 1536–1554. [CrossRef] [PubMed]
46. Lebar, G.; Khojastehnezhad, A.; Peng, Z.; Moeinpour, F.; Siaj, M. Impact of imine-linked covalent organic framework structures on their adsorption performance. *Sep. Purif. Technol.* **2025**, *363*, 132305. [CrossRef]
47. Wang, Y.; Chang, J.-P.; Xu, R.; Bai, S.; Wang, D.; Yang, G.-P.; Sun, L.-Y.; Li, P.; Han, Y.-F. N-Heterocyclic carbenes and their precursors in functionalised porous materials. *Chem. Soc. Rev.* **2021**, *50*, 13559–13586. [CrossRef] [PubMed]
48. Segura, J.L.; Royuela, S.; Mar Ramos, M. Post-synthetic modification of covalent organic frameworks. *Chem. Soc. Rev.* **2019**, *48*, 3903–3945. [CrossRef] [PubMed]
49. Rejali, N.A.; Dinari, M.; Wang, Y. Post-synthetic modifications of covalent organic frameworks (COFs) for diverse applications. *Chem. Commun.* **2023**, *59*, 11631–11647. [CrossRef] [PubMed]
50. Francis Kurisingal, J.; Kim, H.; Hyeak Choe, J.; Seop Hong, C. Covalent organic framework-based catalysts for efficient CO_2 utilization reactions. *Coord. Chem. Rev.* **2022**, *473*, 214835. [CrossRef]
51. Fan, X.; Li, Z. Advances of COFs for photocatalytic application: Water splitting, CO_2 reduction, H_2O_2 production, and organic transformation. *J. Photochem. Photobiol. C Photochem. Rev.* **2025**, *64*, 100712. [CrossRef]
52. Shirani, M.A.; Afshari, M.; Romero-Muñiz, I.; Platero-Prats, A.E.; Dinari, M.; Zamora, F. Designing covalent organic frameworks for organic catalysis: Bridging reticular and molecular chemistry. *J. Mater. Chem. A* **2025**, *13*, 19172–19192. [CrossRef]
53. Alsudairy, Z.; Brown, N.; Campbell, A.; Ambus, A.; Brown, B.; Smith-Petty, K.; Li, X. Covalent organic frameworks in heterogeneous catalysis: Recent advances and future perspective. *Mater. Chem. Front.* **2023**, *7*, 3298–3331. [CrossRef]
54. Feng, X.; Ding, X.; Jiang, D. Covalent organic frameworks. *Chem. Soc. Rev.* **2012**, *41*, 6010–6022. [CrossRef] [PubMed]
55. Ding, S.-Y.; Wang, W. Covalent organic frameworks (COFs): From design to applications. *Chem. Soc. Rev.* **2013**, *42*, 548–568. [CrossRef] [PubMed]
56. Lohse, M.S.; Bein, T. Covalent Organic Frameworks: Structures, Synthesis, and Applications. *Adv. Funct. Mater.* **2018**, *28*, 1705553. [CrossRef]

57. Kandambeth, S.; Dey, K.; Banerjee, R. Covalent Organic Frameworks: Chemistry beyond the Structure. *J. Am. Chem. Soc.* **2019**, *141*, 1807–1822. [CrossRef] [PubMed]
58. Kupgan, G.; Liyana-Arachchi, T.P.; Colina, C.M. NLDFT Pore Size Distribution in Amorphous Microporous Materials. *Langmuir* **2017**, *33*, 11138–11145. [CrossRef] [PubMed]
59. Liu, L.; Corma, A. Metal Catalysts for Heterogeneous Catalysis: From Single Atoms to Nanoclusters and Nanoparticles. *Chem. Rev.* **2018**, *118*, 4981–5079. [CrossRef] [PubMed]
60. Widegren, J.A.; Bennett, M.A.; Finke, R.G. Is It Homogeneous or Heterogeneous Catalysis? Identification of Bulk Ruthenium Metal as the True Catalyst in Benzene Hydrogenations Starting with the Monometallic Precursor, Ru(II)(η6-C6Me6)(OAc)2, Plus Kinetic Characterization of the Heterogeneous Nucleation, Then Autocatalytic Surface-Growth Mechanism of Metal Film Formation. *J. Am. Chem. Soc.* **2003**, *125*, 10301–10310. [CrossRef] [PubMed]
61. Wang, W.; Zheng, A.; Zhao, P.; Xia, C.; Li, F. Au-NHC@Porous Organic Polymers: Synthetic Control and Its Catalytic Application in Alkyne Hydration Reactions. *ACS Catal.* **2014**, *4*, 321–327. [CrossRef]
62. Spitler, E.L.; Koo, B.T.; Novotney, J.L.; Colson, J.W.; Uribe-Romo, F.J.; Gutierrez, G.D.; Clancy, P.; Dichtel, W.R. A 2D Covalent Organic Framework with 4.7-nm Pores and Insight into Its Interlayer Stacking. *J. Am. Chem. Soc.* **2011**, *133*, 19416–19421. [CrossRef] [PubMed]
63. Lukose, B.; Kuc, A.; Heine, T. The Structure of Layered Covalent-Organic Frameworks. *Chem.—A Eur. J.* **2011**, *17*, 2388–2392. [CrossRef] [PubMed]
64. Peris, E. Smart N-Heterocyclic Carbene Ligands in Catalysis. *Chem. Rev.* **2018**, *118*, 9988–10031. [CrossRef] [PubMed]
65. Bañares, M.A. Operando methodology: Combination of in situ spectroscopy and simultaneous activity measurements under catalytic reaction conditions. *Catal. Today* **2005**, *100*, 71–77. [CrossRef]
66. Riduan, S.N.; Zhang, Y.; Ying, J.Y. Conversion of Carbon Dioxide into Methanol with Silanes over N-Heterocyclic Carbene Catalysts. *Angew. Chem. Int. Ed.* **2009**, *48*, 3322–3325. [CrossRef] [PubMed]
67. Kayaki, Y.; Yamamoto, M.; Ikariya, T. N-Heterocyclic Carbenes as Efficient Organocatalysts for CO_2 Fixation Reactions. *Angew. Chem. Int. Ed.* **2009**, *48*, 4194–4197. [CrossRef] [PubMed]
68. Wang, W.; Huang, D.; Zheng, W.; Zhao, X.; He, K.; Pang, H.; Xiang, Y. Construction of Amide-Linked Covalent Organic Frameworks by N-Heterocyclic Carbene-Mediated Selective Oxidation for Photocatalytic Dehalogenation. *Chem. Mater.* **2023**, *35*, 7154–7163. [CrossRef]
69. Pitt, T.A.; Azbell, T.J.; Kim, J.; Shi, Z.; Muller, D.A.; Addicoat, M.A.; Milner, P.J. A Strongly Reducing sp2 Carbon-Conjugated Covalent Organic Framework Formed by N-Heterocyclic Carbene Dimerization. *Angew. Chem. Int. Ed.* **2025**, *64*, e202416480. [CrossRef] [PubMed]
70. DeJesus, J.F.; Sherman, L.M.; Yohannan, D.J.; Becca, J.C.; Strausser, S.L.; Karger, L.F.P.; Jensen, L.; Jenkins, D.M.; Camden, J.P. A Benchtop Method for Appending Protic Functional Groups to N-Heterocyclic Carbene Protected Gold Nanoparticles. *Angew. Chem. Int. Ed.* **2020**, *59*, 7585–7590. [CrossRef] [PubMed]
71. Fogg, D.E.; dos Santos, E.N. Tandem catalysis: A taxonomy and illustrative review. *Coord. Chem. Rev.* **2004**, *248*, 2365–2379. [CrossRef]
72. Wasilke, J.-C.; Obrey, S.J.; Baker, R.T.; Bazan, G.C. Concurrent Tandem Catalysis. *Chem. Rev.* **2005**, *105*, 1001–1020. [CrossRef] [PubMed]
73. Grondal, C.; Jeanty, M.; Enders, D. Organocatalytic cascade reactions as a new tool in total synthesis. *Nat. Chem.* **2010**, *2*, 167–178. [CrossRef] [PubMed]
74. Qu, P.; Cleveland, J.W.; Ahmed, E.; Liu, F.; Dubrawski, S.; Jones, C.W.; Weck, M. Compartmentalisation of molecular catalysts for nonorthogonal tandem catalysis. *Chem. Soc. Rev.* **2022**, *51*, 57–70. [CrossRef] [PubMed]
75. Sullivan, I.; Goryachev, A.; Digdaya, I.A.; Li, X.; Atwater, H.A.; Vermaas, D.A.; Xiang, C. Coupling electrochemical CO_2 conversion with CO_2 capture. *Nat. Catal.* **2021**, *4*, 952–958. [CrossRef]
76. Kamkeng, A.D.N.; Wang, M.; Hu, J.; Du, W.; Qian, F. Transformation technologies for CO_2 utilisation: Current status, challenges and future prospects. *Chem. Eng. J.* **2021**, *409*, 128138. [CrossRef]
77. Shen, Q.; Chen, X.; Tan, Y.; Chen, J.; Chen, L.; Tan, S. Metal-Free N-Formylation of Amines with CO_2 and Hydrosilane by Nitrogen-Doped Graphene Nanosheets. *ACS Appl. Mater. Interfaces* **2019**, *11*, 38838–38848. [CrossRef] [PubMed]
78. Golovacheva, A.A.; Golovkina, A.I.; Otvagina, K.V.; Markin, Z.A.; Smirnova, D.N.; Medov, V.A.; Atlaskin, A.A.; Petukhov, A.N.; Vorotyntsev, A.V.; Kazarina, O.V. Optimization of CO_2 Cycloaddition to Epoxides Using Vinylimidazole-Based Ionic Compounds: Influence of Reaction Parameters on Catalytic Performance. *Ind. Eng. Chem. Res.* **2025**, *64*, 11695–11707. [CrossRef]
79. Pal, D.K.; Ranjane, P.R.; Kulkarni, P.S. Supported ionic liquid catalysts for CO_2-epoxide cycloaddition: A comparative analysis of structure–activity relationships and mechanistic insights across porous frameworks. *Mol. Catal.* **2026**, *601*, 116148. [CrossRef]
80. Yu, B.; Xie, J.-N.; Zhong, C.-L.; Li, W.; He, L.-N. Copper(I)@Carbon-Catalyzed Carboxylation of Terminal Alkynes with CO_2 at Atmospheric Pressure. *ACS Catal.* **2015**, *5*, 3940–3944. [CrossRef]

81. Gunasekar, G.H.; Park, K.; Jung, K.-D.; Yoon, S. Recent developments in the catalytic hydrogenation of CO_2 to formic acid/formate using heterogeneous catalysts. *Inorg. Chem. Front.* **2016**, *3*, 882–895. [CrossRef]
82. Yuan, C.; Fu, S.; Yang, K.; Hou, B.; Liu, Y.; Jiang, J.; Cui, Y. Crystalline C=C and C–C Bond-Linked Chiral Covalent Organic Frameworks. *J. Am. Chem. Soc.* **2021**, *143*, 369–381. [CrossRef] [PubMed]
83. Grunenberg, L.; Lotsch, B.V. Escaping the horns of the COF dilemma. *Matter* **2022**, *5*, 2482–2484. [CrossRef]
84. Mercado, R.; Fu, R.-S.; Yakutovich, A.V.; Talirz, L.; Haranczyk, M.; Smit, B. In Silico Design of 2D and 3D Covalent Organic Frameworks for Methane Storage Applications. *Chem. Mater.* **2018**, *30*, 5069–5086. [CrossRef]
85. Yang, Y.; Ratsch, M.; Evans, A.M.; Börjesson, K. Layered 3D Covalent Organic Framework Films Based on Carbon–Carbon Bonds. *J. Am. Chem. Soc.* **2023**, *145*, 18668–18675. [CrossRef] [PubMed]
86. Lei, P.; Meng, G.; Ling, Y.; An, J.; Szostak, M. Pd-PEPPSI: Pd-NHC Precatalyst for Suzuki–Miyaura Cross-Coupling Reactions of Amides. *J. Org. Chem.* **2017**, *82*, 6638–6646. [CrossRef] [PubMed]
87. Shi, S.; Nolan, S.P.; Szostak, M. Well-Defined Palladium(II)–NHC Precatalysts for Cross-Coupling Reactions of Amides and Esters by Selective N–C/O–C Cleavage. *Acc. Chem. Res.* **2018**, *51*, 2589–2599. [CrossRef] [PubMed]
88. Yang, S.; Zhou, T.; Yu, X.; Nolan, S.P.; Szostak, M. [Pd(NHC)(μ-Cl)Cl]2: The Highly Reactive Air- and Moisture-Stable, Well-Defined Pd(II)-N-Heterocyclic Carbene (NHC) Complexes for Cross-Coupling Reactions. *Acc. Chem. Res.* **2024**, *57*, 3343–3355. [CrossRef] [PubMed]
89. Gordo-Lozano, M.; Matesanz, D.G.; Martínez-Fernández, M.; Almendros, P.; Martínez-Periñán, E.; Segura, J.L.; Cembellín, S. Nile Red-Based Covalent Organic Framework as a Photocatalyst for C–H Bond Functionalization. *ACS Catal.* **2025**, *15*, 10736–10745. [CrossRef] [PubMed]
90. Sun, M.-Y.; Cheung, S.C.; Wang, X.-Z.; Jin, J.-K.; Guo, J.; Li, D.; He, J. Structural Reassignment of Covalent Organic Framework-Supported Palladium Species: Heterogenized Palladacycles as Efficient Catalysts for Sustainable C–H Activation. *ACS Cent. Sci.* **2024**, *10*, 1848–1860. [CrossRef] [PubMed]
91. Sasmal, H.S.; Bag, S.; Chandra, B.; Majumder, P.; Kuiry, H.; Karak, S.; Sen Gupta, S.; Banerjee, R. Heterogeneous C–H Functionalization in Water via Porous Covalent Organic Framework Nanofilms: A Case of Catalytic Sphere Transmutation. *J. Am. Chem. Soc.* **2021**, *143*, 8426–8436. [CrossRef] [PubMed]
92. Pang, H.; Liu, G.; Huang, D.; Zhu, Y.; Zhao, X.; Wang, W.; Xiang, Y. Embedding Hydrogen Atom Transfer Moieties in Covalent Organic Frameworks for Efficient Photocatalytic C−H Functionalization. *Angew. Chem. Int. Ed.* **2023**, *62*, e202313520. [CrossRef] [PubMed]
93. Yang, L.; Wang, J.; Zhao, K.; Fang, Z.; Qiao, H.; Zhai, L.; Mi, L. Photoactive Covalent Organic Frameworks for Catalyzing Organic Reactions. *ChemPlusChem* **2022**, *87*, e202200281. [CrossRef] [PubMed]
94. Wang, L.; Han, C.; Gao, S.; Jiang, J.-X.; Zhang, Y. Covalent Organic Frameworks Enhance Photocatalytic Hydrogen Peroxide Production through Synergistic Effects. *ACS Catal.* **2025**, *15*, 5683–5693. [CrossRef]
95. Tan, D.; Fan, X. COF-Based Photocatalysts for Enhanced Synthesis of Hydrogen Peroxide. *Polymers* **2024**, *16*, 659. [CrossRef] [PubMed]
96. Kranz, C.; Wächtler, M. Characterizing photocatalysts for water splitting: From atoms to bulk and from slow to ultrafast processes. *Chem. Soc. Rev.* **2021**, *50*, 1407–1437. [CrossRef] [PubMed]
97. Sarma, B.B.; Maurer, F.; Doronkin, D.E.; Grunwaldt, J.-D. Design of Single-Atom Catalysts and Tracking Their Fate Using Operando and Advanced X-ray Spectroscopic Tools. *Chem. Rev.* **2023**, *123*, 379–444. [CrossRef] [PubMed]
98. Peng, Y.; Wong, W.K.; Hu, Z.; Cheng, Y.; Yuan, D.; Khan, S.A.; Zhao, D. Room Temperature Batch and Continuous Flow Synthesis of Water-Stable Covalent Organic Frameworks (COFs). *Chem. Mater.* **2016**, *28*, 5095–5101. [CrossRef]
99. Khalil, S.; Alazmi, A.; Gao, G.; Martínez-Jiménez, C.; Saxena, R.; Chen, Y.; Jiang, S.-Y.; Li, J.; Alhashim, S.; Senftle, T.P.; et al. Continuous Synthesis and Processing of Covalent Organic Frameworks in a Flow Reactor. *ACS Appl. Mater. Interfaces* **2024**, *16*, 55206–55217. [CrossRef] [PubMed]
100. Wang, K.; Qiao, X.; Ren, H.; Chen, Y.; Zhang, Z. Industrialization of Covalent Organic Frameworks. *J. Am. Chem. Soc.* **2025**, *147*, 8063–8082. [CrossRef] [PubMed]
101. Danopoulos, A.A.; Simler, T.; Braunstein, P. N-Heterocyclic Carbene Complexes of Copper, Nickel, and Cobalt. *Chem. Rev.* **2019**, *119*, 3730–3961. [CrossRef] [PubMed]

Disclaimer/Publisher's Note: The statements, opinions and data contained in all publications are solely those of the individual author(s) and contributor(s) and not of MDPI and/or the editor(s). MDPI and/or the editor(s) disclaim responsibility for any injury to people or property resulting from any ideas, methods, instructions or products referred to in the content.